Manuscript submitted for consideration by *PLoS Pathogens*

Coronavirus Interferon Antagonists Differentially Modulate the Host Response during Replication in Macrophages

Xufang Deng[1]*, Aaron Volk[1]*, Yafang Chen[2], Kristina R. Kesely[3], Matthew Hackbart[1], Robert C. Mettelman[1], Amornrat O'Brien[1], Andrew D. Mesecar[2,3], and Susan C. Baker[1#]

[1]Department of Microbiology and Immunology, Loyola University Chicago, Stritch School of Medicine, Maywood, IL, [2]Department of Biological Sciences, Purdue University, West Lafayette, IN, [3]Department of Biochemistry, Purdue University, West Lafayette, IN

*These authors contributed equally to this work

[#]Corresponding Author: sbaker1@luc.edu

Abstract

Coronaviruses encode multiple interferon antagonists that modulate the host response to virus replication. Here, we evaluated pathogenesis and host transcription in response to infection with murine coronaviruses encoding independent mutations in two different viral antagonists: the deubiquitinase (DUB) within nonstructural protein 3 and the endoribonuclease (EndoU) within nonstructural protein 15. The virus with reduced ability to deubiquitinate proteins, herein termed the DUBmut virus, was engineered *via* X-ray structure-guided mutagenesis and activates an earlier interferon response than the wild type virus. However, the replication kinetics of DUBmut in cultured cells are similar to wild type virus and pathogenesis in mice is also similar to what was observed during infection with wild type virus. On the other hand, we previously reported that an EndoUmut virus containing an inactivated endoribonuclease activity elicited rapid and robust activation of type I interferon, which limited virus replication and pathogenesis. Here, using a transcriptomics approach, we compared the scope and kinetics of the host response to the wild type, DUBmut, and EndoUmut viruses in infected macrophages. We found that the EndoUmut virus activates a focused response, predominantly involving type I interferons and a subset of interferon-responsive genes, within 12 hours after infection. In contrast, the wild type and DUBmut viruses stimulate upregulation of over 2,800 genes, including activation of unfolded protein response (UPR) pathways and a proinflammatory profile associated with viral pathogenesis. This study highlights the role of viral interferon antagonists in shaping the kinetics and magnitude of the host response during virus infection and demonstrates that inactivation of a dominant viral antagonist, the coronavirus endoribonuclease, dramatically alters the host response in macrophages and the disease process.

Author Summary

Macrophages are an important cell type during coronavirus infections because they "notice" the infection and respond by activating type I interferons, which then act to establish antiviral defenses and limit virus replication. In turn, coronaviruses encode proteins that mitigate the cell's ability to detect virus replication or amplify the interferon response. Here, we evaluated the host macrophage response to two independent mutant coronaviruses: one with a reduced deubiquitinating activity (DUBmut), and the other containing an inactivated endoribonuclease (EndoUmut). We observed a rapid, robust, and focused response to the EndoUmut virus, which was characterized by enhanced expression of interferon and interferon-stimulated genes. These results indicate that coronaviruses utilize EndoU activity for preventing early activation of interferon in macrophages, thereby allowing for viral replication. In contrast, DUBmut elicited a transient interferon response and ultimately activated over 2,800 genes, including many well-known players in pro-inflammatory pathways and the unfolded protein response. These DUBmut-induced pathways are associated with development and progression of significant disease, similar to what is observed during wild type virus infection. This study demonstrates the distinct consequences of mutating different viral interferon antagonists and reveals that intact coronaviral EndoU activity substantially contributes to the ability of coronaviruses to replicate in macrophages.

Introduction

The ability to evade or delay activation of host innate and adaptive immune responses is now recognized as a characteristic of many pathogenic viruses. Viruses from diverse families, including filoviruses [1], poxviruses [2], influenza viruses [3], flaviviruses [4], and coronaviruses [5,6], encode proteins that are not required for viral replication *per se*, but act as modulators of initial,

63 innate host responses or of later, adaptive responses that aim to limit virus replication. By
64 understanding how these viral antagonists regulate the immune response, we can fine-tune the
65 rational design of therapeutics and vaccines to control existing and emerging viral pathogens.

66 Coronaviruses (CoVs) are members of the order *Nidovirales*, which includes enveloped viruses
67 with large (~30kb), positive-sense single-stranded RNA genomes that yield a characteristic nested
68 set of subgenomic mRNAs during replication in the cytoplasm of infected cells [6,7]. The genome
69 organization for coronaviruses is highly conserved, with the 5'-most two-thirds of the genome
70 encoding the replicase polyprotein, followed by sequences encoding the canonical structural
71 proteins: spike, envelope, membrane, and nucleocapsid. Many CoVs contain accessory genes,
72 which are interspersed among the genes for the structural proteins. Although these accessory genes
73 are not necessarily required for virus replication and are, in general, not highly conserved within
74 the virus family, many encode proteins that regulate the host response [8]. Interestingly,
75 coronavirus replicase proteins, which *are* highly conserved, can also act as antagonists to block or
76 delay the innate immune response [9–12]. That a slew of coronavirus-encoded accessory and non-
77 accessory proteins have been shown to shape the host antiviral response suggests that viral-
78 mediated subversion of host defenses is an important element of infection. Here, we focus on two
79 highly conserved domains within the replicase polyprotein—the viral protease/deubiquitinase
80 (DUB) and the endoribonuclease (EndoU)—with the goal of assessing the relative role(s) of each
81 of these enzymatic activities in shaping the pathogenesis of mouse hepatitis virus (MHV), a model
82 murine coronavirus.

83 Coronavirus protease activities are critical for processing the replicase polyprotein. Murine
84 coronavirus MHV encodes three proteases: two papain-like proteases (PLP1 and PLP2) and one
85 chymotrypsin-like protease (3CLpro, also termed Mpro). MHV PLP2 is similar to the single

86 papain-like protease (termed PLpro) of Severe Acute Respiratory Syndrome Coronavirus (SARS-
87 CoV) and Middle East Respiratory Syndrome Coronavirus (MERS-CoV). Bioinformatic analyses
88 and enzymatic studies revealed that the PLpros of SARS-CoV and MERS-CoV are multifunctional
89 proteins that contain protease, deubiquitinase (DUB), and de-ISGylating activities [13–17].
90 However, it has been challenging to study the effects of a mutated DUB on virus replication and
91 pathogenesis because the protease and DUB activities share the same catalytic site, disruption of
92 which is lethal for virus replication. Therefore, it was necessary for us to identify a residue in the
93 MHV protease/DUB-ubiquitin binding domain that can be mutated to result in reduced DUB
94 activity while maintaining sufficient protease activity to allow for proteolytic processing of the
95 replicase polyprotein. In this report, we describe the X-ray structure-guided generation of such a
96 DUB mutant and our subsequent evaluation of its replication and of the host transcriptional
97 response that it elicits during infection. We also sought to expand our understanding of the role of
98 DUB interferon antagonism by comparing it with another recently identified antagonist, the
99 coronavirus endoribonuclease (EndoU).

100 EndoU, a highly conserved enzyme within the coronavirus family, was initially thought to play
101 a role in coronavirus RNA synthesis [18,19]. Recent studies revealed that EndoU acts as an
102 interferon antagonist by preventing activation of host sensors of viral double-stranded RNA
103 (dsRNA) [10,11]. Viruses encoding a catalytically inactive EndoU undergo initial RNA replication
104 but accumulation of viral dsRNA intermediates during replication is detected by host sensors
105 MDA5, PKR, and OAS. Activation of these dsRNA sensors initiates the innate immune response,
106 including activation of type I interferons, interferon-responsive genes, and apoptosis-promoting
107 caspases, all of which collectively limit virus replication. We previously reported that MHV-
108 EndoU mutant viruses are profoundly attenuated in mice and elicit a protective immune response

109 [10]. In the current study, we use transcriptome profiling to evaluate the kinetics of host gene
110 expression in macrophages upon infection with MHV wild type (WT), DUB-mutant, and EndoU-
111 mutant viruses. Our analyses of the respective transcriptional response to each virus reveal
112 significant differences in the kinetics, magnitude, and breadth of host gene expression during
113 infection and provide new information on the extent to which viral interferon antagonists
114 manipulate the overall host response to viral infection.

115 Results

116 Mutation of murine coronavirus papain-like protease 2 ubiquitin-binding domain 117 modulates deubiquitinating activity.

118 To investigate the role of viral deubiquitinating activity in coronavirus replication and
119 pathogenesis, we first needed to identify amino acid residues that, when mutated, result in reduced
120 DUB activity while preserving the enzyme's deISGylating and protease activities, the latter being
121 necessary for viral replication. X-ray structural studies of SARS- and MERS-CoV papain-like
122 protease/DUBs co-crystalized with ubiquitin modified at the c-terminus with a covalent warhead
123 (aldehyde, 3-bromo-propylamine, or propargylamine) allowed for identification of residues that
124 are important for direct interaction with ubiquitin [16,20,21]. Here, we took a slightly different
125 approach and mutated the catalytic cysteine (C1716) of MHV PLP2 to a serine residue and co-
126 crystallized it with free ubiquitin. The X-ray structure of MHV PLP2 (C1716S) in complex with
127 ubiquitin was determined to a resolution of 1.85 Å and an overall R_{free} = 19.6% and R_{work} = 15.8%
128 (PDB: 5WFI). The overall structure of the MHV PLP2-ubiquitin complex is similar to other
129 PLP2/PLpro ubiquitin-bound structures (Fig 1A). Ubiquitin binds within the palm region and is
130 gripped by the zinc-fingers motif while the c-terminus extends into the active site.

131 Next, we aligned the primary amino acid sequence of the MHV PLP2 domain with the
132 SARS-CoV and MERS-CoV papain-like protease domains (Fig 1E). The sequence alignment and
133 X-ray structure of the MHV PLP2–ubiquitin complex were then analyzed in conjunction with the
134 previous structural and mutagenesis studies on SARS- and MERS-CoV to identify candidate
135 residues that could be mutated to render a loss of DUB activity *in vitro*. From this analysis, we
136 identified three residues (R1803, D1772, F1812) in MHV PLP2 that form direct interactions with
137 ubiquitin (Fig 2B-D). Two of the side chain guanidinium nitrogens of R1803 form direct hydrogen
138 bonds with the backbone carbonyl oxygen of A46 in ubiquitin (Fig 1B). The two side chain
139 carboxylate oxygens of D1772 in MHV PLP2 interact with ubiquitin by forming direct bonds with
140 each of the guanidinium nitrogens of R42 and with one of the guanidinium nitrogens of R72 (Fig
141 1C). Finally, F1812 forms Van der Waals contacts with the side chains of I44 and V70 and the
142 delta-carbon of R42 of ubiquitin (Fig 1D).

143 To identify a mutant MHV PLP2 enzyme that retains protease activity but exhibits reduced
144 DUB and/or deISGylating activity, we performed site-directed mutagenesis on each of the residues
145 (R1803, D1772, F1812) by changing each to an alanine to disrupt interactions with ubiquitin. Each
146 mutant enzyme was expressed, purified, and tested for its ability to hydrolyze three substrates: z-
147 RLRGG-AMC, Ub-AMC, and ISG15-AMC. The activity of each mutant enzyme toward each
148 substrate relative to the wild type enzyme is shown in Fig 2A. All three mutants retained their
149 ability to hydrolyze the peptide substrate but each mutant had altered specificity toward Ub-AMC
150 and ISG15-AMC substrates. Mutation of F1812 resulted in a substantial decrease in hydrolysis of
151 both Ub-AMC and ISG15-AMC (Class I), whereas mutation of R1803 resulted in loss of activity
152 only toward ISG15-AMC (Class II), and mutation of D1772 resulted in loss of activity only toward
153 Ub-AMC (Class III).

154 Since one of the primary goals of this study is to understand the contribution of DUB
155 activity to viral replication and pathogenesis, we next focused on quantitating further the effects
156 of the D1772A mutant on the steady-state kinetic parameters of MHV PLP2 toward the three
157 different substrates (Fig 2B). The RLRGG-AMC peptide substrate is often used as surrogate of
158 the viral polyprotein substrate and the kinetic data in Fig 2B show that this substrate is still well-
159 recognized and cleaved by the D1772A mutant. In fact, we observed a small rate enhancement in
160 the catalytic efficiency (i.e., k_{cat}/K_m) compared to the wild type enzyme.

161 The Ub-AMC substrate, on the other hand, is poorly recognized and cleaved by the
162 D1772A compared to the wild type enzyme. The wild type enzyme normally interacts strongly
163 with Ub-AMC with a K_m value of 0.67 μM. However, mutation of D1772 to an alanine
164 significantly disrupts the interaction with ubiquitin, making it impossible to saturate MHV PLP2
165 under normal experimental conditions (Fig 2B). The net result is a significant reduction in the
166 catalytic efficiency (k_{cat}/K_m) compared to the wild type enzyme, which was the goal of these trials.

167 The kinetic response of MHV PLP2 toward another substrate, ISG15-AMC, was also
168 determined. ISG15 is an important ubiquitin-like modifier that is upregulated and used to ISGylate
169 host proteins during viral infection. A number of viruses, including coronaviruses, engender
170 ISGylation during infection but the function(s) and importance of this activity are not clear. For
171 MHV, neither the wild type nor the D1772A mutant PLP2 enzyme can be saturated with ISG15-
172 AMC, suggesting weak binding with this ubiquitin-like modifier (Fig 2B). Moreover, the R1772A
173 mutation does not disrupt the interaction with ISG15 but in fact enhances it to some degree. A
174 potential explanation for the observed selective disruption of ubiquitin binding stems from our
175 analysis of a primary sequence alignment of ubiquitin and ISG15 and the residues that interact
176 with D1772 (Fig 2C). The interaction between MHV PLP2 D1772 and the R42 residue in human

177 and mouse ubiquitin is absent in human and mouse ISG15 since this residue is a tryptophan in
178 human and mouse ISG15. Therefore, in line with our observations, D1772A mutation would not
179 be expected to alter ISG15 binding. In contrast to R42, residue R72 is conserved in both ubiquitin
180 and ISG15 and its interaction with MHV PLP2 for ubiquitin is likely weaker than that with ISG15.

181 The *in vitro* biochemical studies presented here support the notion that we are able to use
182 a structure-guided approach to uncouple the DUB enzymatic activity from MHV PLP2 while
183 preserving the peptide hydrolysis and deISGylating activities of PLP2. Next, we focused on
184 comparing the activity of the mutant enzyme to its wild type counterpart for the ability to remove
185 Flag-tagged-ubiquitin conjugated to host proteins in cultured cells (Fig 3A). We found that in cells,
186 wild type PLP2 exhibits robust DUB activity and removes ubiquitin modifications from multiple
187 cellular proteins. On the other hand, the PLP2-D1772A mutant exhibits reduced DUB activity,
188 similar to that of the previously documented catalytic cysteine to alanine mutant, PLP2-CA [22].
189 To determine if this impaired DUB activity altered the ability of PLP2/DUB to act as an interferon
190 antagonist, we transfected cells with RIG-I, an interferon-luciferase reporter, and either wild type
191 or mutant PLP2 and measured luciferase activity at 18 hours post-transfection. In agreement with
192 previous reports, we find that wild type PLP2/DUB acts as an interferon antagonist, reducing
193 reporter activity by 50-80%. In contrast, PLP2-D1772A is unable to significantly reduce interferon
194 activation in this assay despite similar expression levels of the wild type and mutant versions of
195 the protein (Fig 3B). We also evaluated the protease activity of the enzymes in cells using two
196 independent *trans*-cleavage assays and found that the wild type and DUB-mutant enzymes produce
197 similar levels of cleaved products. These results indicate that the D1772A substitution did not alter
198 protease activity (Fig 3C and D), in agreement with the *in vitro* kinetic results described above

199 (Fig 2). Together, these studies reveal that aspartic acid residue 1772 of MHV-PLP2 is important
200 for DUB-mediated interferon antagonism, but not for protease activity.

201 Since the D1772A substitution did not impact protease activity, we reasoned that we should
202 be able to recover infectious virus containing this substitution, thereby allowing us to determine if
203 the mutation has any effect on viral replication kinetics and interferon antagonism in the context
204 of the live virus. We generated the mutant virus *via* reverse genetics [23], performed full genome
205 sequencing to verify the genotype (2 nucleotide changes at positions 5525 and 5526, resulting in
206 D1772A substitution in the replicase polyprotein), and designated the virus as DUBmut. Upon
207 evaluating virus replication of the DUBmut virus by performing a growth kinetics experiment in
208 parallel with wild type virus, we found that DUBmut replicates with essentially identical kinetics
209 as the wild type in a murine astrocytoma cell line (DBT cells) (Fig 4A). These results are consistent
210 with previous studies of coronavirus interferon antagonists, which showed in many cell lines that
211 viral-mediated interferon antagonism is not essential for virus replication [10,11].

212 To determine if the impaired DUB activity of the DUBmut virus had an effect on interferon
213 antagonism, we infected primary bone marrow-derived macrophages (BMDMs) and evaluated
214 viral replication kinetics and levels of interferon mRNA and protein. We observed significant
215 activation of interferon alpha (IFNα) mRNA expression (Fig 4A) that is coupled with release of
216 IFNα protein into the supernatant, as detected by ELISA (Fig 4B). We show that this activation of
217 IFNα is dependent on expression of pattern recognition receptor MDA5 (Fig 4D), in agreement
218 with previous reports [10,11]. To our surprise, we found that replication of DUBmut is not
219 impaired relative to wild type in BMDMs, as measured by level of nucleocapsid RNA (Fig 4E)
220 and evaluation of infectious virus particle production over time in the kinetics assay (Fig 4F).
221 These results demonstrate that an elevated interferon response is generated during replication of

222 the DUBmut virus, but that this interferon profile is not associated with reduced production of
223 infectious particles in either DBT cells or BMDMs.

224 **Disrupting DUB activity is mildly attenuating to coronavirus pathogenesis in mice.**

225 To complement our *in vitro* studies, we next sought to determine whether loss of DUB
226 activity and the observed activation of interferon during DUBmut infection in macrophages is
227 associated with an attenuated phenotype in mice. To test this, we inoculated mice intra-peritoneally
228 with 6×10^4 plaque-forming units (pfu) of the designated virus and measured viral titer in the liver
229 and spleen at the indicated days post-infection (dpi). We detected similar levels of infectious
230 particles at 3 dpi, but reduced levels of infectious particles in the livers and spleens of DUBmut-
231 infected mice at 5 dpi (Fig 5A). Similar pathology in liver sections was observed at 3 and 5 dpi
232 (Fig 5B). These results suggest that the DUBmut virus is mildly attenuated compared to the wild
233 type virus when evaluated using the intraperitoneal route of infection. We also used the more
234 sensitive intracranial infection model to evaluate pathogenesis and found similar lethality among
235 WT and DUBmut-infected mice (Fig 5C). We were surprised at the similarities between wild type
236 and DUBmut infection *in vivo* since our previous study involving inactivation of a different viral
237 interferon antagonist, EndoU, revealed profound attenuation and rapid clearance of an EndoU-
238 mutant virus from infected mice [10]. Having shown that the DUBmut and the EndoUmut viruses
239 each activate an innate immune response, we expected that infection of mice with either mutant
240 virus would lead to similar outcomes. Therefore, as our expectations for the DUBmut virus were
241 in stark contrast to what we observed, we next performed transcriptome profiling of infected
242 macrophages at multiple time points in order to build a more complete understanding of the host
243 response to the wild type virus, DUBmut virus, and the highly attenuated EndoUmut virus.

244 **Transcriptome profiling reveals differences in kinetics and magnitude of host responses to**
245 **mutant viruses.**

246 BMDMs were infected with the designated virus and total RNA was harvested for RNA-
247 seq transcriptome profiling at 3, 6, 9, and 12 hours post-infection (hpi). Using the RNA-seq data,
248 we identified differentially expressed genes by applying a cutoff of at least 4-fold elevated
249 expression in wild type-infected cells at 12 hpi over mock ($q < 0.05$). We then utilized Cluster 3.0
250 software to visualize overall patterns of gene expression between all groups across all time points
251 (Fig 6). These analyses reveal significant differences in overall patterns of gene expression
252 between the EndoUmut-infected cells and wild type virus-infected cells, whereas the gene
253 expression profile induced by the DUBmut virus is remarkably similar to wild type virus infection
254 (Fig 6). More specifically, 2,879 genes are significantly transcriptionally activated (>4-fold, $q <$
255 0.05) in wild type- and DUBmut-infected macrophages by 12 hpi when compared to mock-
256 infected macrophages. Interestingly, our analyses also identified a subset of 231 genes, indicated
257 by the bracket in Figure 6, that were most highly upregulated in EndoUmut-infected cells. It is
258 important to note that these genes were also induced during WT and DUBmut infections, but not
259 to the same magnitude as detected in the EndoUmut-infected cells. We next sought to functionally
260 cluster these 231 genes as a means of investigating the respective host transcriptional response to
261 each mutant virus.

262 **EndoUmut infection activates genes associated with an antiviral response.**

263 Using an online tool called Database for Annotation, Visualization and
264 Integrated Discovery (DAVID) to cluster the 231 genes bracketed in Figure 6 based on functional
265 similarities [24,25], we find that the protein products of these genes are predominantly involved
266 in antiviral and signaling pathways. Notably, the DAVID analyses reveal a subset of 30 unique
267 genes, including several interferon isoforms, which are clustered together into statistically

268 significant pathways associated with the immune response and signaling cascades (Fig 7A).
269 Interestingly, the heat map of these genes reveals a similar temporal trend in upregulation of IFN
270 gene expression during infection with each of the three viruses; however, this expression profile
271 is by far the most pronounced in the EndoUmut-infected cells. In this heatmap view, as in Figure
272 6, it is difficult to ascertain any difference in expression of IFN genes between wild type- and
273 DUBmut-infected cells; therefore, to obtain more information on the kinetics of transcriptional
274 activation between groups, we quantitated the reads associated with each gene and graphically
275 display the normalized read counts in Figure 7B (also see Supplemental Fig 1). Using this method
276 of plotting the read counts over time, we detected statistically significant transcriptional
277 upregulation of IFN gene expression in the DUBmut-infected cells, in agreement with the data
278 presented in Figure 4. However, the magnitude of DUBmut-induced IFN gene expression was
279 dwarfed by IFN activation in EndoUmut-infected cells. EndoUmut-infected macrophages
280 exhibited markedly elevated levels of IFN transcripts as early as 9 hpi. By 12 hpi, expression of
281 the genes bracketed in Fig 6 upon EndoUmut infection was significantly higher than during WT
282 or DUBmut infection, with our assay detecting 1,000-10,000 more reads per gene in the
283 EndoUmut-infected cells. This focused response to EndoUmut is successful in limiting virus
284 replication in cultured macrophages, as demonstrated in our previous report [10]. Notably, we
285 evaluated the transcriptional response during the first 12 hpi, prior to the onset of apoptosis, which
286 we and others have shown to occur in BMDMs upon EndoUmut infection [10,11].

287 **Wild type and DUBmut coronavirus replication activate the unfolded protein response and**
288 **host response to cell damage.**

289 In contrast to the robust, but focused, antiviral gene expression response detected in
290 EndoUmut-infected macrophages, we uncovered a complex response involving 2,879 genes in
291 both WT- and DUBmut-infected macrophages by 12 hpi. The overall patterns of expression of

292 these genes in DUBmut- and WT-infected BMDMs are strikingly similar (Figs 6 and 7). We
293 therefore propose that the comparable outcomes of infection observed in DUBmut- and WT-
294 infected mice are a consequence of transcriptionally similar host responses to each virus. Using
295 DAVID-based functional clustering, we identified multiple statistically significant functional
296 clusters within this set of 2,879 genes that are implicated in signaling cascades, the general immune
297 response, and transcriptional regulation. These analyses reveal substantial upregulation in
298 expression of many proinflammatory genes, including well-known players TNF, IL-6, IL-1b,
299 CXCL-10, CXCL-11, and CCL3 (Fig 8). We noted significant differences in the activation of these
300 genes associated with a proinflammatory response in BMDMs infected with either the wild type
301 virus or DUBmut compared to those infected with EndoUmut. Potent activation of these genes by
302 12 hpi may stimulate recruitment of inflammatory mediators directed at tissue repair [26]. In
303 addition to this pro-inflammatory signature, wild type- and DUBmut-infected cells also exhibit
304 hallmarks of activation of the host unfolded protein response (UPR).

305 UPR pathways are activated when unfolded proteins accumulate in the endoplasmic
306 reticulum (ER), at which point the host cell initiates measures to resolve this overload [26]. In the
307 context of virus infection, viral glycoproteins accumulate in the ER, triggering the release of BiP
308 from three sensor proteins: IRE1, ATF6, and PERK. Activation of these sensors triggers signaling
309 cascades resulting in transcriptional activation of genes encoding ER chaperones and proteins
310 involved in lipid synthesis and amino acid transport (Fig 9A). Based on our analyses of differential
311 gene expression, we report significant transcriptional upregulation of multiple genes associated
312 with activation of ER sensors IRE1, ATF6, and PERK, such as Edem1, Hspa5 (encoding BiP
313 protein), and Ddit3 (encoding CHOP), in response to virus replication, with the most robust
314 response detected in cells infected with the wild type or DUBmut virus (Fig 9 B, C, and D).

315 Overall, these differential gene expression analyses in macrophages reveal similar host responses
316 to the wild type and DUBmut viruses that include activation of UPR pathways and
317 proinflammatory genes, whereas a distinct transcriptional profile during infection with the
318 EndoUmut virus is predominately defined by a focused, robust antiviral response.

319 Discussion

320 Here, we report that inactivation of a coronaviral interferon antagonist, EndoU, profoundly
321 alters the host response to viral replication in macrophages. We find that the EndoUmut virus
322 elicits a rapid, robust, and specific antiviral response that was effective in limiting virus replication.
323 In contrast, our data show that the WT and DUBmut viruses ultimately elicit very similar host
324 responses that are both characteristic of an unfolded protein response and consistent with a
325 proinflammatory profile that is associated with viral pathogenesis [27]. The results from the
326 DUBmut-infected macrophages indicate that the mere induction of type I IFN is not a sufficient
327 marker for attenuation of the virus. Instead, these results suggest that the *timing* and the *magnitude*
328 of the host antiviral response are critical for determining the outcome of infection in macrophages.
329 Our observation that the EndoUmut virus induces an earlier and more profoundly elevated type I
330 interferon response than even the DUBmut virus implies that there is a threshold of IFN expression
331 that must be breached before the cell mounts an effective antiviral response.

332 The structure-guided approach used to generate the DUBmut virus allowed for
333 characterization of three different classes of mutant enzymes: Class I, deficient in both DUB and
334 de-ISGylating activity; Class II, deficient in de-ISGylating activity only; and Class III, deficient
335 in DUB activity but competent in protease and de-ISGylating activity. We utilized three unique
336 biochemical substrates, each with a conjugated fluorescent AMC reporter, to evoke the multi-

337 functional activities of PLP2. Activity against the z-RLRGG-AMC peptide substrate represents
338 the polyprotein processing activity of MHV PLP2, while UB-AMC and ISG15-AMC stimulate
339 the deubiquitinating and deISGylating activities of the enzyme, respectively. The kinetic data for
340 the D1772A DUBmut hydrolysis of the z-RLRGG-peptide provided in Figure 2B indicate that the
341 polyprotein processing ability of this mutant is likely not affected by the D1772A substitution. The
342 deISGylating ability of the enzyme is also not affected. In contrast, the mutant enzyme's
343 deubiquitinating activity is significantly reduced relative to wild type, which is most likely due to
344 a lowered binding affinity for ubiquitin as the enzyme could not be saturated with Ub-AMC as a
345 substrate.

346 We were able to reproduce the enzymatic profile of the purified PLP2-D1772A mutant
347 protein when we expressed it in cell culture (Fig 3). Therefore, our finding that the DUBmut virus
348 containing the PLP2-D1772A substitution activates an elevated antiviral response in macrophages
349 compared to the wild type virus, but that this antiviral state results in only mild attenuation of
350 disease in mice relative to WT infection, was unexpected. Previous studies demonstrated that
351 ubiquitin has important roles in both the activation and the attenuation of innate antiviral pathways
352 [28]; therefore, we anticipated a more remarkable phenotype for a DUB-mutant virus. We can
353 imagine several possible explanations for our findings. First, it is possible that viral DUB activity
354 has a relatively minor role in shaping pathogenesis in this system. In fact, our recent studies using
355 SARS-CoV and SARS-related CoVs found that the papain-like protease domain/DUB is a
356 virulence trait that varies among members of the SARS-coronavirus species [9]. In that study, we
357 found that replacing the SARS PLP2/DUB domain with a SARS-related PLP2/DUB domain
358 reduced the ability of that virus to antagonize the innate immune response. Together, this previous
359 report in conjunction with the current study support the concept that different PLP2/DUB domains

360 may have distinct effects on antagonism of the innate immune response depending on the virus
361 and the host cell type. Another possibility is that the DUB-mutant virus we generated may not have
362 been sufficiently debilitated in its DUB activity to result in altered pathogenesis. We found that it
363 was difficult to recover viable DUB-mutant viruses; indeed, this D1772A mutant was the sole
364 viable DUB-mutant representative of our many attempts. Because an elevated interferon response
365 was elicited from DUBmut-infected cells, this mutant virus fulfilled our criteria demonstrating the
366 inactivation of an interferon antagonist. However, we speculate that if we are able to recover
367 mutants that exhibit a range of DUB activity, we may be able to more fully assess the role of DUB
368 activity as a contributor to coronaviral pathogenesis. Despite these caveats, the MHV DUB-mutant
369 generated in this study did exhibit a reproducible phenotype of eliciting an elevated interferon
370 response in infected macrophages that was associated with mild attenuation of pathogenesis with
371 reduced titers in the livers and spleens of mice at day 5 post-infection. Overall, we conclude that
372 DUB activity is indeed a virulence trait, but not a major driver of virulence for MHV. Our results
373 support the concept that multiple viral factors likely work in concert to shape and ultimately limit
374 the innate immune response to coronavirus replication.

375 The other remarkable finding from this study was the distinct transcriptional profile elicited
376 by the EndoUmut virus during infection of bone marrow-derived macrophages compared to the
377 profiles of wild type- and DUBmut-infected cells (Fig 6). We detected elevated levels of interferon
378 and interferon-responsive genes as early as 6-9 hpi, with EndoUmut-infected cells exhibiting by
379 far the highest expression levels of these genes. We and others found that an antiviral response to
380 EndoUmut infection results in activation of apoptosis, which subsequently limits virus replication
381 in cell culture and in infected mice [10,11]. The current study indicates that screening MHV
382 mutants in interferon-responsive cells may be an effective approach to identifying strains that

383 stimulate a robust innate immune response, which may then restrict virus replication in animals.
384 Previous studies of coronavirus-encoded interferon antagonists focused on evaluating the host
385 transcriptional response to infection at later time points (such as 24 and 48 hpi) and in a variety of
386 cell types or the tissues of infected animals. For example, a study comparing infection of mice
387 with wild type SARS-CoV versus a virus containing a mutation in the interferon antagonist nsp16,
388 termed the dNSP16 CoV, revealed that the transcriptional profile in the lungs of the dNSP16-
389 infected mice mirrored the response to wild type virus [12]. However, combining the dNSP16
390 mutation with a mutation in another interferon antagonist, ExoN, was shown to reduce disease in
391 mice and elicit protective immunity. It would be interesting to determine if the transcriptional
392 profile elicited by the double mutant SARS-CoV is altered compared to wild type virus,
393 particularly at early times after infection. A study of MERS-CoV comparing the host response to
394 wild type virus with the response to a mutant virus containing deleted accessory open reading
395 frames (MERS-CoV dORF3-5) provides evidence of significant differences in the early
396 transcriptional responses to infection in Calu3 2B4 cells [29]. This study revealed that MERS-CoV
397 dORF3-5 infection prompted earlier (7, 12, and 24 hpi) and more robust type I and type III
398 interferon responses, and that the mutant virus was more sensitive than wild type to pre-treatment
399 with interferon. The MERS-CoV interferon antagonist mutant virus was attenuated in mice and
400 elicited a protective response against subsequent lethal challenge. For coronaviruses, one difficulty
401 that arises when evaluating the role(s) of viral-mediated modulation of the host response is that
402 multiple viral proteins, including both structural and nonstructural proteins, have been shown to
403 antagonize the innate immune response *in vitro* and/or *in vivo*. These include: nsp16-2'O MTase,
404 nsp14-ExoN, nsp1, nsp7, E protein, N protein, M protein, SARS-CoV-ORF6, MERS-CoV-ORF3-
405 5, MERS-CoV-4a, and MERS-CoV-4b [12,29–33]. Each of these interferon antagonists may play

406 either a cell- or tissue-type specific role, or act in concert with other factors during viral replication
407 to mitigate the innate immune response. Further studies are needed to fully understand if all or
408 only a subset of these antagonists must be silenced to generate an effective, live-attenuated vaccine.
409 The results presented here and from the study of the MERS-CoV dORF3-5 mutant virus indicate
410 that inactivating interferon antagonists and screening for an early and robust antiviral
411 transcriptional profile may represent an efficient and informative approach to evaluating live-
412 attenuated vaccine candidate strains for existing and emerging coronaviruses.

413 Our results demonstrating upregulation of the unfolded protein response (UPR) in response
414 to wild type and DUBmut coronavirus replication confirm and extend the work of earlier studies
415 that documented activation of the ER sensors PERK, IRE1, and ATF-6 during coronavirus
416 infection [32,34,35]. Heavy utilization of the endoplasmic reticulum for generating coronavirus
417 replication complexes and of the ER-Golgi intermediate compartment for assembling virus
418 particles places a substantial load on the host translational machinery during infection. Host
419 sensors IRE1, ATF-6, and PERK are situated in the ER to sense and respond to such overload by
420 prompting upregulated expression of genes encoding ER chaperones, amino acid transporters, and
421 activators of lipid biosynthesis. Ironically, many of these proteins ultimately facilitate virus
422 replication and assembly. Notably, it has been demonstrated that UPR pathways that promote
423 apoptosis are blocked during coronavirus replication [32,34]. The ability of viruses to modulate
424 the UPR has important implications for the innate immune response to such viruses because the
425 UPR has been shown to attenuate antiviral defenses by way of degrading the type I interferon
426 receptor [36]. To our knowledge, the results presented here provide the first transcriptomic
427 evidence of UPR activation in coronavirus-infected macrophages, underlining an important role
428 for UPR pathways in the coronavirus life cycle. Our observation that EndoUmut-infected

429 macrophages exhibit significantly lower expression of several genes involved in UPR pathways
430 compared with wild type- and DUBmut-infected cells is consistent with the reduced levels of virus
431 replication detected in EndoUmut-infected macrophages.

432 The notion of inactivating viral interferon antagonists as a means of generating live-
433 attenuated vaccines is supported by recent reports of screening for inactivation of influenza A
434 virus-encoded interferon antagonists [3], as well as studies that revealed that the classic vaccine
435 strain of yellow fever virus encodes an interferon antagonist in the NS5 protein [37]. For
436 coronaviruses, it is not yet clear if disabling a single interferon antagonist, such as the highly
437 conserved EndoU, will be sufficient to attenuate viruses that infect different cell types in different
438 species. Promisingly, our studies of a coronavirus that causes lethal disease in piglets, porcine
439 epidemic diarrhea virus (PEDV), revealed that inactivation of EndoU activity is associated with
440 attenuated disease [38]. However, additional work is needed to evaluate potential reversion of
441 EndoU mutant viruses and to determine if inactivating multiple interferon antagonists is an
442 effective approach for generating safe and effective live-attenuated coronavirus vaccines.

443 Materials and Methods

444 Ethics Statement

445 The mouse experiment in this study was carried out in accordance with the
446 recommendations in the Guide for the Care and Use of Laboratory Animals of the National
447 Institutes of Health. The experimental protocol was reviewed and approved by the Institutional
448 Animal Care and Use Committee (IACUC) at Loyola University Chicago (IACUC#: 2016-029).
449 C57BL/6 female mice were purchased from The Jackson Laboratory and maintained in the
450 Comparative Medicine Facility of Loyola University Chicago. Mice were consistently monitored

451 for signs of distress over the course of the experiments to be removed from the experiment and
452 euthanized using carbon dioxide inhalation to prevent unnecessary suffering.

453 **Cells**

454 Human embryonic kidney (HEK) 293T cells were purchased the from American Type
455 Culture Collection (ATCC, # CRL-11268) and maintained in DMEM (#10-017-CV, Corning)
456 containing 10% fetal calf serum (FCS) and supplemented with 1% nonessential amino acids, 1%
457 HEPES, 2% L-glutamine, 1% sodium pyruvate, and 1% penicillin/streptomycin. DBT cells were
458 cultured in MEM (#61100-061, ThermoFisher) supplemented with 5% FCS, 2% L-glutamine, and
459 10% Tryptose Phosphate Broth (TPB). The 17Cl-1 cell line was maintained in DMEM containing
460 5% FCS. Baby hamster kidney cells expressing the MHV receptor (BHK-R) were kindly provided
461 by Mark Denison (Vanderbilt University Medical Center) and maintained in DMEM supplemented
462 with 10% FCS, 2% L-glutamine, and 0.8 μg/mL G418. Bone marrow-derived macrophages
463 (BMDMs) were prepared and cultured as described previously [10].

464 **Plasmids and mutagenesis**

465 The sequence of the PLP2 domain (amino acids 1525-1911 of MHV pp1ab) in frame with
466 a V5 epitope tag was codon-optimized, synthesized by Genscript (Piscataway, NJ) (sequence
467 available upon request), and cloned into pCAGGS vector. For mutagenesis, an overlapping PCR
468 strategy was used with synthetic primers (sequences available upon request). The introduced
469 mutations were verified by sequencing. The RIG-I and nsp2/3-GFP expression plasmid was kindly
470 provided Ralph Baric (University of North Carolina). The IFNβ-Luc reporter plasmid was a gift
471 of John Hiscott (Jewish General Hospital, Montreal, Canada). The Flag-Ub plasmid was kindly
472 provided by Adriano Marchese (University of Wisconsin-Milwaukee).

473 **MHV PLP2 wild type and mutant purification, kinetics, and X-ray structure**

474 The wild type, C1716S, D1772A, R1803A, and F1812A mutant enzymes were expressed
475 and purified similar to our previously published methods except that the MHV PLP2 construct
476 used here (amino acids N1609 to N1909) was absent the DPUP domain [39]. Crystallization and
477 X-ray structure determination details will be published elsewhere. Steady-state kinetic studies on
478 the wild type, D1772A, R1803A, and F1812A mutant enzymes with substrates Z-RLRGG-AMC
479 (where Z is a carboxybenzyl protecting group), Ubiquitin-AMC, and ISG15-AMC were performed
480 as described previously [39]. X-ray structural coordinates have been deposited under PDB code
481 5WFI. Structure figures were generated with the software program UCSF Chimera [40].

482 **Protease and deubiquitinating activity assays**

483 To determine the protease activity of PLP2, HEK293T cells grown to 70% confluency in
484 24-well plates (Corning) were transfected using *Trans*IT-LT1 (MIR2300, Mirus) according to the
485 manufacturer's protocol. For the protease activity assay, HEK293T cells were transfected with 25
486 ng nsp2/3-GFP plasmid and 200 ng pCAGGS-PLP2-V5 expression plasmids (wild type and
487 mutant). To determine deubiquitinating activity of the proteins, cells were transfected with 200 ng
488 Flag-Ub plasmid and pCAGGS-PLP2-V5 expression plasmids (wild type and mutant). Cells were
489 lysed 24 h post-transfection with 100 μL of lysis buffer (comprising 20 mM Tris [pH 7.5], 150
490 mM NaCl, 1mM EGTA, 1mM EDTA, 1% Triton X-100, 2.5 mM sodium pyrophosphate, 1mM β-
491 glycerophosphate, 1mM sodium orthovanadate, 1 μg/mL leupeptin, and 1mM
492 phenylmethylsulfonyl fluoride). Whole cell lysates were separated by SDS-PAGE and transferred
493 to PVDF membrane in transfer buffer (0.025M Tris, 0.192M glycine, 20% methanol) for 1 hour
494 at 60 Volts at 4°C. Following this, the membrane was blocked using 5% dried skim milk in TBST
495 buffer (0.9% NaCl, 10mM Tris-HCl, pH7.5, 0.1% Tween 20) overnight at 4°C. The membrane
496 was incubated with either polyclonal rabbit anti-GFP antibody (A11122, Life Technologies) for

497 the protease assay, or mouse anti-flag (F3165, Sigma) for the DUB assay. The membrane was then
498 washed three times for 15 minutes in TBST buffer followed by incubation with either secondary
499 donkey anti-rabbit-HRP antibody (711-035-152, Jackson ImmunoResearch) or goat anti-mouse-
500 HRP antibody (1010-05, SouthernBiotech). Then the membrane was washed three more times for
501 15 minutes in TBST buffer. Detection was performed using Western Lighting Chemiluminescence
502 Reagent Plus (PerkinElmer) and visualized using a FluoroChemE Imager (Protein Simple). The
503 expression of PLP2, β-actin, and calnexin were probed with mouse anti-V5 antibody (R960,
504 ThermoFisher), mouse anti–β-actin (A00702, Genscript), or mouse anti-calnexin antibody (2433S,
505 Cell Signaling), respectively.

506 **Biosensor live cell assay**

507 The protease activity of PLP2 was also assessed using a biosensor live cell assay as
508 described previously [41]. Briefly, HEK293T cells in a 96 black-wall plate were transfected with
509 37.5 ng pGlo-RLKGG construct and 50 ng PLP2 expression plasmids. GloSensor (E1290,
510 Promega) reagent diluted in DMEM+10% FCS was added at 18 hpi. Plates were read using a
511 luminometer (Veritas) every hour over a course of 5 hours.

512 **Generating DUB-mutant MHV**

513 We used a previously described reverse genetics system of MHV-A59 [23] to generate the
514 DUB-mutant virus. Briefly, the nucleotides coding for the Asp-1772 of the PLP2 domain were
515 mutated *via* site-directed mutagenesis. Viral genomic RNA from *in vitro* transcription of ligated
516 cDNA fragments using a mMESSAGE mMACHINE T7 Transcription Kit (AM1344, Thermal
517 Fisher) was electroporated into BHK-R cells. Cell supernatants were collected as viral stock
518 following observation of cytopathic effects. Rescued virus was plaque-purified, propagated on
519 BHK-R cells, and titrated on 17Cl-1 cells. The stock virus was subjected to full-genome

520 sequencing and the sequences were aligned to the parental strain, with the intended engineered
521 mutation detected and no additional mutations detected (Kansas State University Diagnostic
522 Laboratory).

523 **Growth kinetics**

524 DBT cells or BMDMs were infected with wild type icMHV-A59 or DUB-mutant virus at
525 a multiplicity of infection (MOI) of 1 in serum-free medium. After a one-hour incubation, the
526 inoculum was replaced with fresh, complete medium. Cell culture supernatants were collected at
527 indicated time points and titrated by plaque assay on 17Cl-1 cells. Titers were obtained from three
528 independent assays for each sample. Graphs of virus kinetics were generated using Prism software
529 (GraphPad Software).

530 **Quantification of IFNα production by RT-qPCR and ELISA**

531 BMDMs in a 12-well plate were mock-infected or infected with MHV at a MOI of 1. At
532 indicated time points, monolayer cells were collected for RNA extraction and cell culture
533 supernatants were harvested for ELISA analysis. To determine IFN-α11, β-actin, or MHV-A59 N
534 gene mRNA levels, total RNA was extracted from collected cells using a RNeasy Mini Kit (74104,
535 Qiagen). The first strand cDNA was synthesized from an equal amount of RNA using Rt2 HT First
536 Strand Kit (330401, Qiagen). qPCR was then performed with specific primers for mouse IFN-α11
537 (PPM03050B-200, Qiagen), mouse β-actin (PPM02945B-200, Qiagen), or MHV-A59 N gene
538 using RT2 SYBR Green qPCR Mastermix (330502, Qiagen) in the Bio-Rad CFX96 system. The
539 thermocycler was set as follows: one step at 95°C (10 min), 40 cycles of 95°C (15 s), 60°C (1 min)
540 and plate read, one step at 95 °C (10 s), and a melt curve from 65°C to 95°C at increments of
541 0.5°C/0.05s. Samples were evaluated in triplicate and data are representative of three independent
542 experiments. The levels of mRNA were reported relative to β-actin mRNA and expressed as $2^{-\Delta CT}$

543 [$\Delta C_T = C_{T(gene\ of\ interest)} - C_{T(\beta\text{-}actin)}$]. The secreted amount of IFN-α in culture supernatants was
544 assayed using a mouse IFN-α ELISA kit (BMS6027, eBioscience) according to the
545 manufacturer's instructions.

546 **Mouse experiments**

547 Evaluation of MHV pathogenesis in laboratory mouse was previously described [10,42].
548 Briefly, for intracranial infections, six-week-old C57BL/6 female mice were inoculated with 600
549 pfu of virus in 20 μL PBS. Infected mice were monitored for body weight daily and euthanized
550 when weight loss surpassed 25%. Statistical analyses of survival rate were performed using the
551 log-rank test. For intraperitoneal infection, each mouse was injected with 6×10^4 pfu of virus in 100
552 μL PBS. Organs were collected at indicated time points and evaluated for viral burden. Liver
553 pathology was evaluated using H&E staining by the Tissue Processing Core Facility at Loyola
554 University Chicago.

555 **RNA-seq data analysis pipeline**

556 Raw RNA-seq reads were subjected to analysis using Galaxy's online platform to generate
557 differential gene expression data between infection groups [43]. Reads were clipped to remove
558 any residual unique barcode sequences that were added during preparation of each sample for
559 sequencing. Clipped reads were concatenated to combine multiple files per sample into a single
560 file per sample. These files were groomed to ensure that all reads were in Sanger FASTQ format.
561 FASTQ reads were aligned to the GRCm38 Ensembl build of the C57BL/6J mouse genome using
562 HISAT2 aligner, which locates the region of the genome to which each read corresponds, resulting
563 in an output BAM file [44]. All reads that did not align to the mouse genome (i.e., reads that
564 originated from viral RNA) were discarded. The BAM files contained the alignment information
565 for each read in that sample and were used as inputs into featureCounts, which quantifies the

566 number of reads in each sample that corresponds to each gene in the mouse genome [45]. Finally,
567 the output count data from featureCounts was used as the input for DESeq2 to calculate differential
568 expression for each gene across all samples and treatment groups. DESeq2 was used to generate
569 normalized count values for each gene in all samples [46]. These normalized counts are intended
570 to correct for size differences between samples that might otherwise skew differential expression
571 calculations if some samples contained substantially different numbers of total reads. The
572 normalized count values were plotted and visualized in heat maps, generated using R, and line
573 graphs, generated using Prism software. Submission of all RNA seq data is in progress with NCBI
574 GEO, and an accession number will be provided prior to publication of this manuscript.

575 **Identifying differentially expressed genes (DEGs)**

576 To identify and analyze differentially expressed genes (DEGs) between infection groups,
577 we used as a starting point the list of DEGs between mock- and WT MHV-infected BMDMs at 12
578 hpi that was generated as an output by DESeq2. This list of genes was filtered based on the
579 statistical significance associated with the fold-change differential expression value. A q-value
580 (aka adjusted p-value, calculated by DESeq2 for each gene in each comparison using the
581 Benjamini-Hochberg procedure) of < 0.05 was chosen as the cutoff for statistical significance;
582 genes whose differential upregulation values did not meet this cutoff in WT-MHV-infected
583 BMDMs at 12 hpi compared with mock-infected cells were removed from the list [46]. Next, a
584 differential expression magnitude cutoff of > 4 was applied to the remaining genes. Genes that
585 were not more highly expressed by at least 4-fold in WT-MHV-infected cells at 12 hpi compared
586 to mock were removed from the list. After applying these cutoffs, 2,879 genes remained and were
587 arranged in order of most- to least-highly upregulated in WT-MHV-infected cells at 12 hpi
588 compared to mock. Cluster 3.0 software was then used to apply mathematical clustering to the z-
589 score-standardized log2-normalized mean normalized count values associated with each gene in

590 each time point and infection group [47]. Specifically, the default settings—the similarity metric
591 "Pearson correlation (uncentered)" and the clustering method "centroid linkage"—were applied to
592 the list of 2,879 genes and the corresponding expression values for each gene across all samples
593 to produce a hierarchically clustered gene list based on how similar or different the expression
594 patterns were between groups of genes across all samples. This new list of clustered genes and
595 their associated expression values were then visualized as a heatmap using Java TreeView
596 software.

597 Acknowledgments

598 We thank Dr. Qunfeng Dong for assistance with the bioinformatic analyses. This work was
599 supported by the National Institutes of Health (NIH) grant R01 AI085089 (to SCB and ADM).
600 MH and RCM were supported by NIH T32 Training Grant for Experimental Immunology
601 (#AI007508) and RCM was supported by the Arthur J. Schmitt Dissertation Fellowship in
602 Leadership and Service (Arthur J. Schmitt Foundation). Crystallization and DNA sequencing were
603 partially supported by the Purdue Center for Cancer Research Macromolecular Crystallography
604 and DNA Sequencing Shared Resources, which are supported by NIH grant P30 CA023168.

605 Author Contributions

606 Conceptualization: XD, AV, ADM and SCB. Investigation: XD, AV, YC, KRK, MH,
607 RCM, AO. Formal Analysis: XD, AV, YC, KRK, MH, RCM, AO, ADM and SCB. Writing –
608 Original Draft Preparation: XD, AV, MH, ADM and SCB. Writing – Review & Editing: with
609 comments from XD, AV, MH, RCM, AO, ADM and SCB. Visualization: XD, AV, YC, KRK,
610 MH, AO, ADM and SCB. Funding Acquisition and Supervision: ADM and SCB.

611 References

612 1. Chatterjee S, Basler CF, Amarasinghe GK, Leung DW. Molecular Mechanisms of Innate
613 Immune Inhibition by Non-Segmented Negative-Sense RNA Viruses. J Mol Biol.
614 2016;428: 3467–3482. doi:10.1016/j.jmb.2016.07.017
615 2. Stuart JH, Sumner RP, Lu Y, Snowden JS, Smith GL. Vaccinia Virus Protein C6 Inhibits
616 Type I IFN Signalling in the Nucleus and Binds to the Transactivation Domain of STAT2.
617 PLoS Pathog. 2016;12: 1–24. doi:10.1371/journal.ppat.1005955
618 3. Du Y, Shi Y, Zhang T-H, Dai L, Gong D, Brar G, et al. Genome-wide identification of
619 interferon-sensitive mutations enables influenza vaccine design. Science (80-). 2018;359:
620 290–296. doi:10.1126/science.aan8806
621 4. Best SM. The Many Faces of the Flavivirus NS5 Protein in Antagonism of Type I
622 Interferon Signaling. J Virol. 2017;91: 1–14. doi:10.1128/jvi.01970-16
623 5. Kindler E, Thiel V. To sense or not to sense viral RNA-essentials of coronavirus innate
624 immune evasion. Curr Opin Microbiol. 2014;20: 69–75. doi:10.1016/j.mib.2014.05.005
625 6. Perlman S, Netland J. Coronaviruses post-SARS: update on replication and pathogenesis.
626 Nat Rev Microbiol. 2009;7(6): 439–50. doi:10.1038/nrmicro2147
627 7. Cui J, Li F, Shi Z-L. Origin and evolution of pathogenic coronaviruses. Nat Rev
628 Microbiol. 2019;17: 181–192. doi:10.1038/s41579-018-0118-9
629 8. Totura AL, Baric RS. SARS coronavirus pathogenesis: host innate immune responses and
630 viral antagonism of interferon. Curr Opin Virol. 2012;2: 264–75.
631 doi:10.1016/j.coviro.2012.04.004
632 9. Niemeyer D, Mösbauer K, Klein EM, Sieberg A, Mettelman RC, Mielech AM, et al. The
633 papain-like protease determines a virulence trait that varies among members of the SARS-
634 coronavirus species. Poon L, editor. PLOS Pathog. 2018;14: e1007296.

635 doi:10.1371/journal.ppat.1007296
636 10. Deng X, Hackbart M, Mettelman RC, O'Brien A, Mielech AM, Yi G, et al. Coronavirus
637 nonstructural protein 15 mediates evasion of dsRNA sensors and limits apoptosis in
638 macrophages. Proc Natl Acad Sci U S A. 2017;114: E4251–E4260.
639 doi:10.1073/pnas.1618310114
640 11. Kindler E, Gil-Cruz C, Spanier J, Li Y, Wilhelm J, Rabouw HH, et al. Early
641 endonuclease-mediated evasion of RNA sensing ensures efficient coronavirus replication.
642 Perlman S, editor. PLOS Pathog. 2017;13: e1006195. doi:10.1371/journal.ppat.1006195
643 12. Menachery VD, Gralinski LE, Mitchell HD, Dinnon KH, Leist SR, Yount BL, et al.
644 Combination attenuation offers strategy for live-attenuated coronavirus vaccines. J Virol.
645 2018;92: e00710-18. doi:10.1128/JVI.00710-18
646 13. Barretto N, Jukneliene D, Ratia K, Chen Z, Mesecar AD, Baker SC. The papain-like
647 protease of severe acute respiratory syndrome coronavirus has deubiquitinating activity. J
648 Virol. 2005;79(24): 15189–15198. doi:10.1128/JVI.79.24.15189
649 14. Lindner HA, Fotouhi-Ardakani N, Lytvyn V, Lachance P, Sulea T, Ménard R. The
650 papain-like protease from the severe acute respiratory syndrome coronavirus is a
651 deubiquitinating enzyme. J Virol. 2005;79(24): 15199–208. doi:10.1128/JVI.79.24.15199-
652 15208.2005
653 15. Ratia K, Saikatendu KS, Santarsiero BD, Barretto N, Baker SC, Stevens RC, et al. Severe
654 acute respiratory syndrome coronavirus papain-like protease : Structure of a viral
655 deubiquitinating enzyme. Proc Natl Acad Sci U S A. 2006;103(15): 5717–22.
656 16. Ratia K, Kilianski A, Baez-Santos YM, Baker SC, Mesecar A. Structural basis for the
657 ubiquitin-linkage specificity and deISGylating activity of SARS-CoV papain-like

658 protease. PLoS Pathog. 2014;10: e1004113. doi:10.1371/journal.ppat.1004113
659 17. Mielech AM, Kilianski A, Baez-Santos YM, Mesecar AD, Baker SC. MERS-CoV papain-
660 like protease has deISGylating and deubiquitinating activities. Virology. 2014;450–451:
661 64–70. doi:10.1016/j.virol.2013.11.040
662 18. Snijder EJ, Bredenbeek PJ, Dobbe JC, Thiel V, Ziebuhr J, Poon LLM, et al. Unique and
663 conserved features of genome and proteome of SARS-coronavirus, an early split-off from
664 the coronavirus group 2 lineage. J Mol Biol. 2003;331: 991–1004. doi:10.1016/S0022-
665 2836(03)00865-9
666 19. Ivanov KA, Hertzig T, Rozanov M, Bayer S, Thiel V, Gorbalenya AEA, et al. Major
667 genetic marker of nidoviruses encodes a replicative endoribonuclease. Proc Natl Acad Sci
668 U S A. 2004;101: 12694–12699. doi:10.1073/pnas.0403127101
669 20. Bailey-Elkin BA, Knaap RCM, Johnson GG, Dalebout TJ, Ninaber DK, van Kasteren PB,
670 et al. Crystal structure of the MERS coronavirus papain-like protease bound to ubiquitin
671 facilitates targeted disruption of deubiquitinating activity to demonstrate its role in innate
672 immune suppression. J Biol Chem. 2014;289: 34667–82. doi:10.1074/jbc.M114.609644
673 21. Békés M, van der Heden van Noort GJ, Ekkebus R, Ovaa H, Huang TT, Lima CD.
674 Recognition of Lys48-Linked Di-ubiquitin and Deubiquitinating Activities of the SARS
675 Coronavirus Papain-like Protease. Mol Cell. 2016;62: 572–585.
676 doi:10.1016/j.molcel.2016.04.016
677 22. Mielech AM, Deng X, Chen Y, Kindler E, Wheeler DL, Mesecar AD, et al. Murine
678 coronavirus ubiquitin-like domain is important for papain-like protease stability and viral
679 pathogenesis. J Virol. 2015;89: 4907–4917. doi:10.1128/JVI.00338-15
680 23. Yount B, Denison MR, Weiss SR, Ralph S, Baric RS. Systematic assembly of a full-

681 length infectious cDNA of mouse hepatitis virus strain A59. J Virol. 2002;76: 11065–
682 11078. doi:10.1128/JVI.76.21.11065
683 24. Huang DW, Sherman BT, Lempicki RA. Bioinformatics enrichment tools: paths toward
684 the comprehensive functional analysis of large gene lists. Nucleic Acids Res. 2009;37: 1–
685 13. doi:10.1093/nar/gkn923
686 25. Huang DW, Sherman BT, Lempicki RA. Systematic and integrative analysis of large gene
687 lists using DAVID bioinformatics resources. Nat Protoc. 2009;4: 44–57.
688 doi:10.1038/nprot.2008.211
689 26. Grootjans J, Kaser A, Kaufman RJ, Blumberg RS. The unfolded protein response in
690 immunity and inflammation. Nat Rev Immunol. 2016;16: 469–484.
691 doi:10.1038/nri.2016.62
692 27. Channappanavar R, Fehr AR, Vijay R, Mack M, Zhao J, Meyerholz DK, et al.
693 Dysregulated type I interferon and inflammatory monocyte-macrophage responses cause
694 lethal pneumonia in SARS-CoV-infected mice. Cell Host Microbe. 2016;19: 181–193.
695 doi:10.1016/j.chom.2016.01.007
696 28. Heaton SM, Borg NA, Dixit VM. Ubiquitin in the activation and attenuation of innate
697 antiviral immunity. J Exp Med. 2016;213: 1–13. doi:10.1084/jem.20151531
698 29. Menachery VD, Mitchell HD, Cockrell AS, Gralinski LE, Yount BL, Graham RL, et al.
699 MERS-CoV Accessory ORFs Play Key Role for Infection and Pathogenesis. Racaniello
700 VR, editor. MBio. 2017;8: e00665-17. doi:10.1128/mBio.00665-17
701 30. Frieman M, Yount B, Heise M, Kopecky-Bromberg SA, Palese P, Baric RS. Severe acute
702 respiratory syndrome coronavirus ORF6 antagonizes STAT1 function by sequestering
703 nuclear import factors on the rough endoplasmic reticulum/Golgi membrane. J Virol.

704 2007;81: 9812–24. doi:10.1128/JVI.01012-07
705 31. Frieman M, Ratia K, Johnston RE, Mesecar AD, Baric RS. Severe acute respiratory
706 syndrome coronavirus papain-like protease ubiquitin-like domain and catalytic domain
707 regulate antagonism of IRF3 and NF-kappaB signaling. J Virol. 2009;83(13): 6689–705.
708 doi:10.1128/JVI.02220-08
709 32. Rabouw HH, Langereis MA, Knaap RCM, Dalebout TJ, Canton J, Sola I, et al. Middle
710 East respiratory coronavirus accessory protein 4a inhibits PKR-mediated antiviral stress
711 responses. PLoS Pathog. 2016;12: e1005982. doi:10.1371/journal.ppat.1005982
712 33. Menachery VD, Gralinski LE, Mitchell HD, Dinnon KH, Leist SR, Yount BL, et al.
713 Middle East Respiratory Syndrome Coronavirus Nonstructural Protein 16 Is Necessary for
714 Interferon Resistance and Viral Pathogenesis. mSphere. 2017;2: e00346-17.
715 doi:10.1128/mSphere.00346-17
716 34. Bechill J, Chen Z, Brewer JW, Baker SC. Coronavirus infection modulates the unfolded
717 protein response and mediates sustained translational repression. J Virol. 2008;82: 4492–
718 501. doi:10.1128/JVI.00017-08
719 35. Fung T, Liao Y, Liu D. Regulation of Stress Responses and Translational Control by
720 Coronavirus. Viruses. 2016;8: 184. doi:10.3390/v8070184
721 36. Liu J, HuangFu W-C, Kumar KGS, Qian J, Casey JP, Hamanaka RB, et al. Virus-Induced
722 Unfolded Protein Response Attenuates Antiviral Defenses via Phosphorylation-Dependent
723 Degradation of the Type I Interferon Receptor. Cell Host Microbe. 2009;5: 72–83.
724 doi:10.1016/J.CHOM.2008.11.008
725 37. Laurent-Rolle M, Morrison J, Rajsbaum R, Macleod JML, Pisanelli G, Pham A, et al. The
726 Interferon Signaling Antagonist Function of Yellow Fever Virus NS5 Protein Is Activated

727 by Type I Interferon. Cell Host Microbe. 2014;16: 314–327.
728 doi:10.1016/j.chom.2014.07.015
729 38. Deng X, van Geelen A, Buckley AC, O'Brien A, Pillatzki A, Lager KM, et al.
730 Coronavirus Endoribonuclease Activity in Porcine Epidemic Diarrhea Virus Suppresses
731 Type I and Type III Interferon Responses. J Virol. 2019;93: e02000-18.
732 doi:10.1128/JVI.02000-18
733 39. Chen Y, Savinov SN, Mielech AM, Cao T, Baker SC, Mesecar AD. X-ray structural and
734 functional studies of the three tandemly linked domains of non-structural protein 3 (nsp3)
735 from murine hepatitis virus reveal conserved functions. J Biol Chem. 2015;290: 25293–
736 306. doi:10.1074/jbc.M115.662130
737 40. Pettersen EF, Goddard TD, Huang CC, Couch GS, Greenblatt DM, Meng EC, et al. UCSF
738 Chimera?A visualization system for exploratory research and analysis. J Comput Chem.
739 2004;25: 1605–1612. doi:10.1002/jcc.20084
740 41. Kilianski A, Mielech A, Deng X, Baker SC. Assessing Activity and Inhibition of MERS-
741 CoV Papain-like and 3C-like Proteases Using Luciferase-based Biosensors. J Virol.
742 2013;87(21): 11955–11962. doi:10.1128/JVI.02105-13
743 42. Deng X, StJohn SE, Osswald HL, O'Brien A, Banach BS, Sleeman K, et al.
744 Coronaviruses resistant to a 3C-like protease inhibitor are attenuated for replication and
745 pathogenesis, revealing a low genetic barrier but high fitness cost of resistance. J Virol.
746 2014;88: 11886–11898. doi:10.1128/JVI.01528-14
747 43. Afgan E, Baker D, Batut B, van den Beek M, Bouvier D, Čech M, et al. The Galaxy
748 platform for accessible, reproducible and collaborative biomedical analyses: 2018 update.
749 Nucleic Acids Res. 2018;46: W537–W544. doi:10.1093/nar/gky379

750 44. Kim D, Langmead B, Salzberg SL. HISAT: a fast spliced aligner with low memory
751 requirements. Nat Methods. 2015;12: 357–60. doi:10.1038/nmeth.3317
752 45. Liao Y, Smyth GK, Shi W. featureCounts: an efficient general purpose program for
753 assigning sequence reads to genomic features. Bioinformatics. 2014;30: 923–930.
754 doi:10.1093/bioinformatics/btt656
755 46. Love MI, Huber W, Anders S. Moderated estimation of fold change and dispersion for
756 RNA-seq data with DESeq2. Genome Biol. 2014;15: 550. doi:10.1186/s13059-014-0550-
757 8
758 47. de Hoon MJL, Imoto S, Nolan J, Miyano S. Open source clustering software.
759 Bioinformatics. 2004;20: 1453–1454. doi:10.1093/bioinformatics/bth078
760

761 ## Supporting Information Legends

762 **Figure S1. Plots of normalized read counts of IFN and IFN-stimulated genes identified by**
763 **functional clustering as shown in Figure 7.** (A) Normalized read count values for the most
764 highly expressed genes are plotted as line graphs. (B) Normalized read count values for genes
765 with less than 100 reads at 12 hours post-infection. Plotted are the average normalized counts for
766 each gene in EndoUmut- (red), DUBmut- (green), WT-MHV- (blue), and mock-infected (black)
767 BMDMs infection groups over all 4 time points.

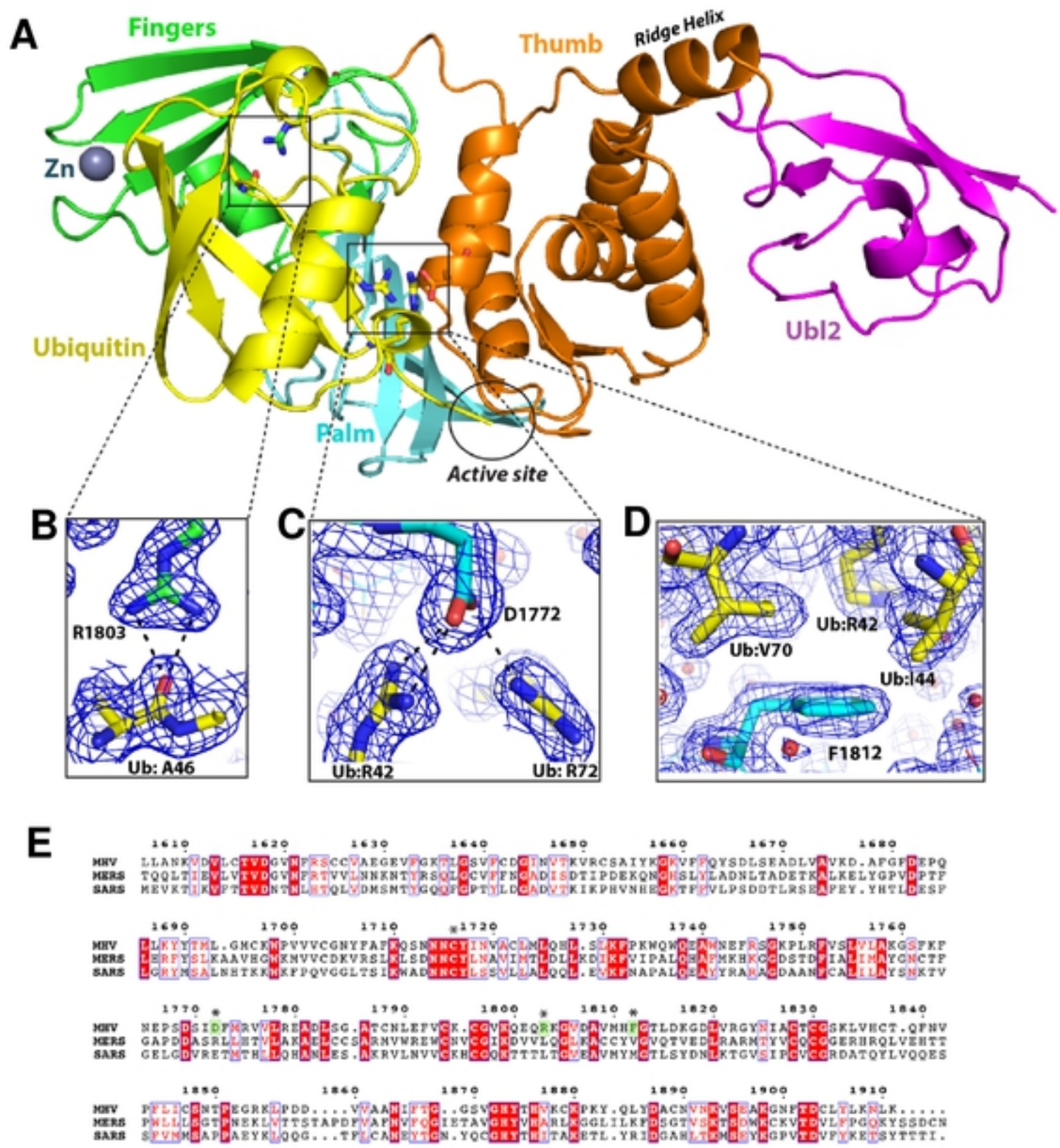

Figure 1. X-ray structure of the MHV PLP2-Ubiquitin complex and residues involved in ubiquitin binding. (A) Overall structure of MHV PLP2-C194S-Ub complex. Domains are color coded: Ub in yellow, Ubl2 domain of PLP2 in purple, thumb domain in orange, palm domain in cyan, and fingers domain in green. Residue D1772 of PLP2 is located outside of the active site, which is circled in black. (B) Hydrogen bond interactions between MHV PLP2 R1803 and the backbone of ubiquitin A46. (C) Binding interactions between MHV PLP2 D1772 and two arginine residues (R42 and R72). (D) Hydrophobic interactions between F1812 of MHV PLP2 and ubiquitin residues I44 and V70. The 2Fo-Fc maps (blue) surrounding the residues are contoured at 1σ in each panel. The PDB coordinates for the MHV PLP2-C1716S-Ub complex have been deposited under PDB Code 5WFI. (E) Sequence alignment of coronavirus papain-like protease/deubiquitinating domains from MHV (1606-1911 aa, accession # AAX23975), SARS (1541-1854 aa, accession # ACZ72209), and MERS (1480-1803 aa, accession # AHY21467). Numbering is based on MHV sequence. Amino acids mutated in this study are indicated with an asterisk and those that bind ubiquitin are boxed in green. The sequence alignment was created using ESPript.

A

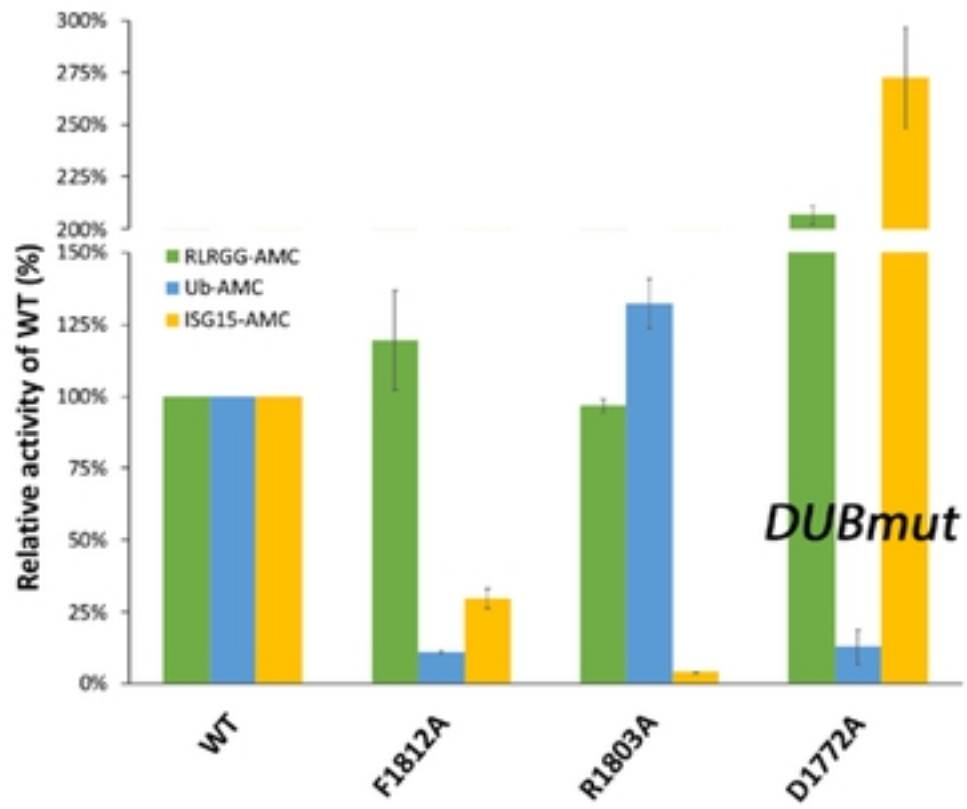

B

	RLRGG-AMC	Ub-AMC	ISG15-AMC
Wild type			
k_{cat} (min^{-1})	-	42.4 ± 1.2	-
K_m (μM)	-	0.67 ± 0.06	-
k_{cat}/K_m ($min^{-1}\mu M^{-1}$)	[a]2.4 ± 0.04 x10^{-3}	63 ± 5.6	[a]2.4 ± 0.07
D1772A			
k_{cat} (min^{-1})	-	-	-
K_m (μM)	-	-	-
k_{cat}/K_m ($min^{-1}\mu M^{-1}$)	[a]5.1 ± 0.07 x10^{-3}	[a]7.8 ± 0.2	[a]7.4 ± 0.06

[a]Saturation with substrate(s) could not be achieved.

C

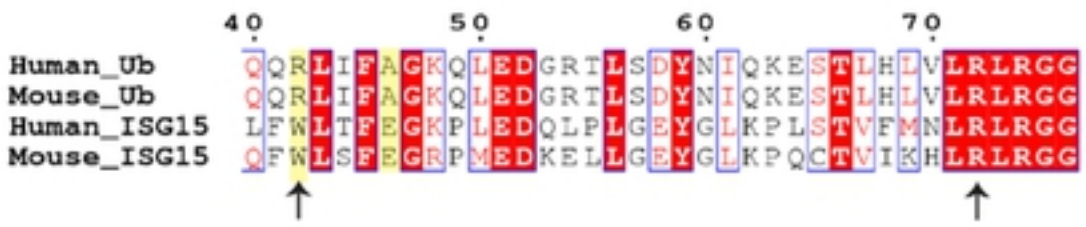

Figure 2. Structure-guided mutagenesis of MHV PLP2 reveals that D1772A disrupts ubiquitin binding and reduces DUB activity. (A) Relative kinetic activities of three mutant MHV PLP2 enzymes toward three substrates: z-RLRGG-AMC (green), Ub-AMC (blue), and ISG15-AMC (yellow) compared to the wild type enzyme. (B) Steady–state kinetic parameters for wild type and D1772A mutant enzymes. (C) Sequence alignment of Ub and ISG15 from human and mouse generated by Clustal Omega. The two arginine residues of Ub (R42 and R72) that interact with D1772 are indicated by arrows. R72 is conserved between Ub and ISG15, whereas R42 (shaded in yellow) is only present in Ub. Accession numbers: Human_Ub, 1ubq; Mouse_Ub, P62991; Human_ISG15, AAH09507; Mouse_ISG15, AAI09347. The sequence alignment was created using ESPript.

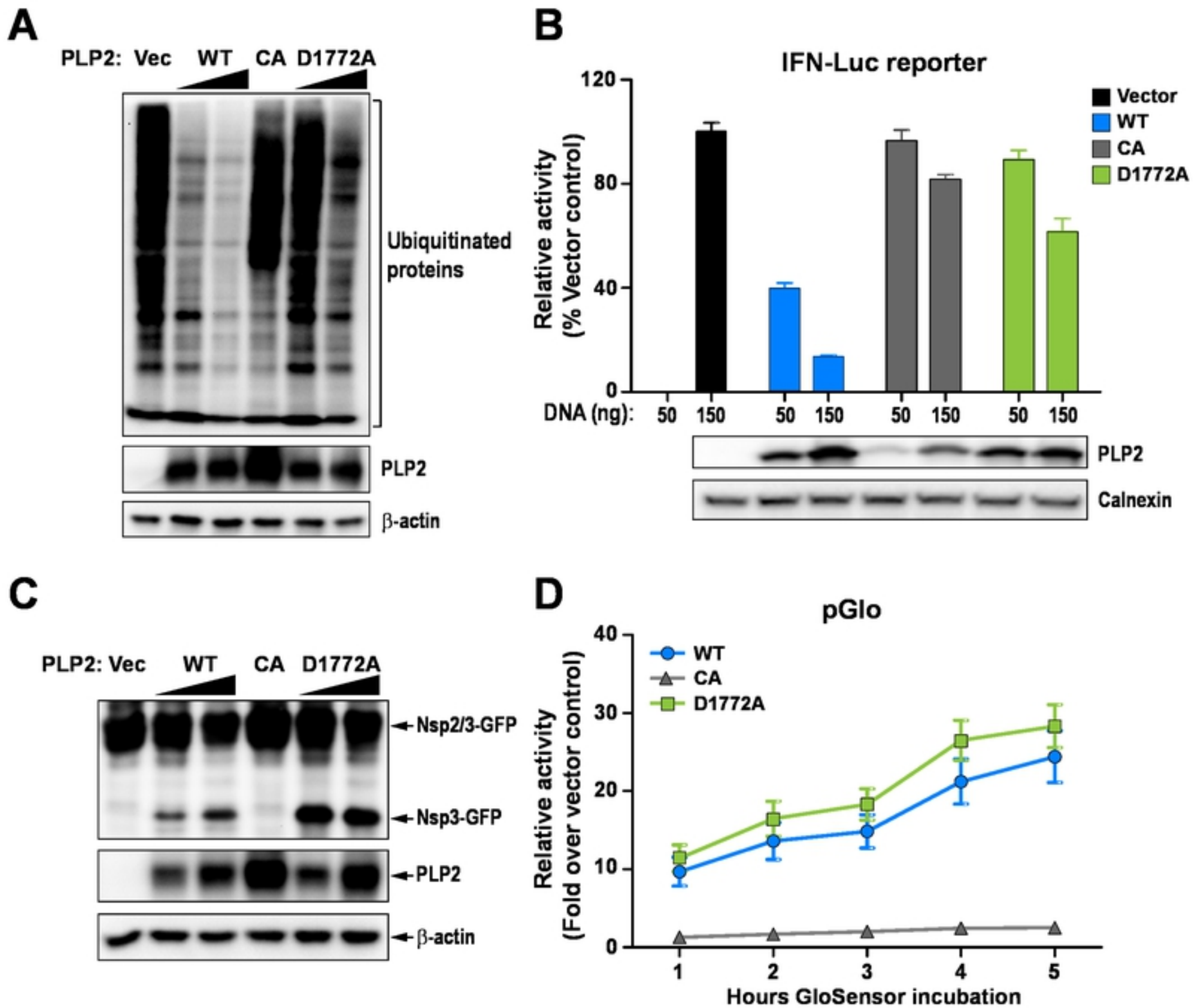

Figure 3. D1772A substitution in the coronavirus papain-like protease Ub-binding site reduces DUB activity and interferon antagonism without reducing protease activity. (A) Western blot assessing the DUB activity of PLP2. (B) IFN antagonism of PLP2 was determined using an IFN-luciferase reporter stimulated by N-RIG-I expression. Protease activity was evaluated using (C) a *trans*-cleavage assay that detects the cleaved products by western blot and (D) a pGlo biosensor assay which is activated by PLP2-mediated cleavage of the substrate. Data are representative of at least two independent experiments. Data in (B) and (D) are presented as means ± SD.

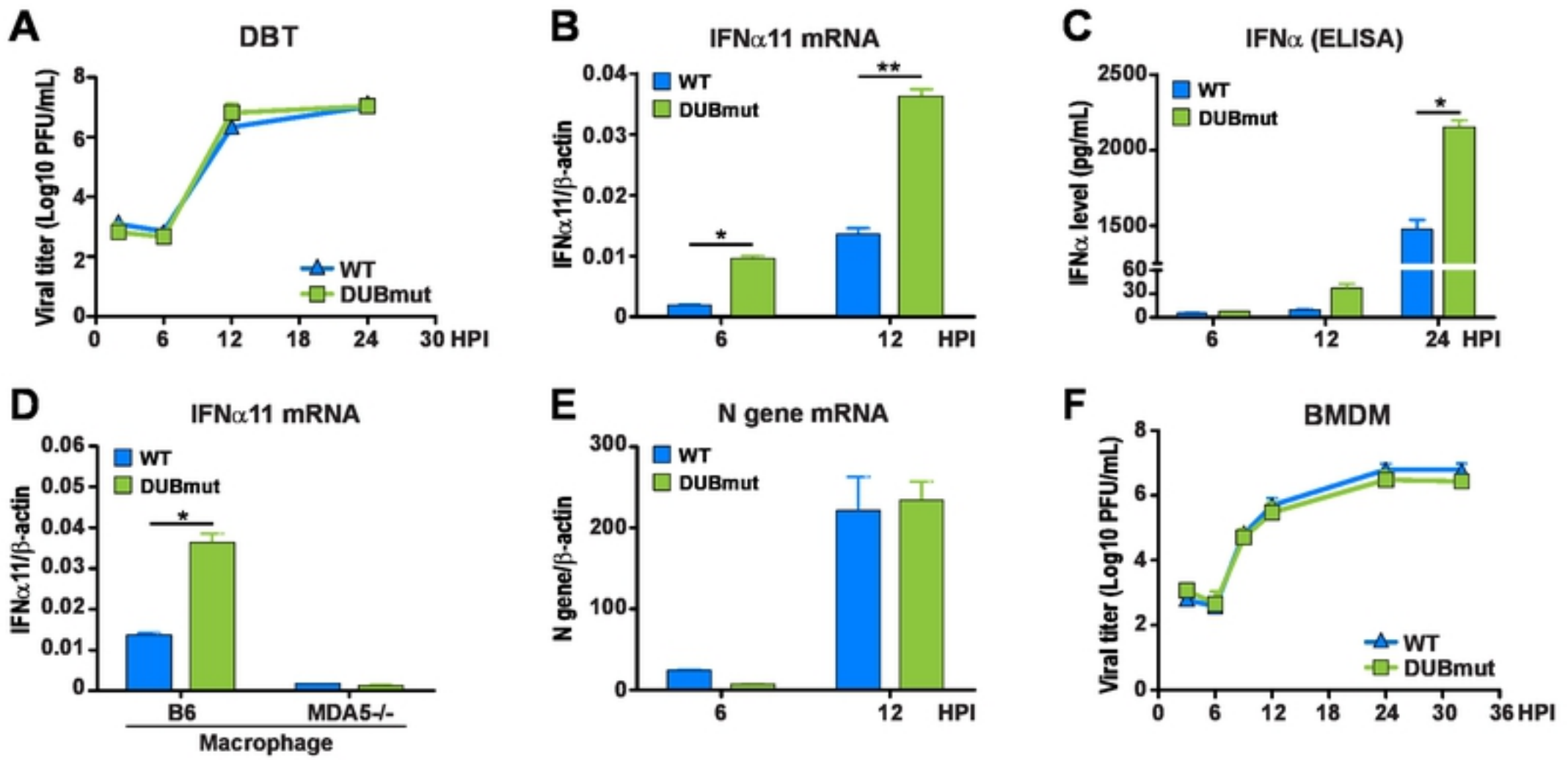

Figure 4. Evaluating the replication kinetics of, and level of interferon activation by, WT MHV and DUBmut in cell culture. (A) Replication kinetics of WT and DUBmut virus in DBT cells. (B) IFNα11 mRNA levels in WT- and DUBmut-infected BMDMs were assessed at indicated time points by qRT-PCR. (C) IFNα protein levels in the supernatants of infected BMDMs were evaluated at the times indicated. (D) Comparison of IFNα11 levels in B6 versus MDA5-/- BMDMs at 12 hours post-infection (HPI). (E) Assessing levels of viral nucleocapsid (N) mRNA by qRT-PCR. (F) Replication kinetics of WT and DUBmut virus in BMDM cells. Data are representative of at least two independent experiments and are presented as means ± SD. Data in (B) and (C) were statistically analyzed using unpaired t-tests. *, $p < 0.05$; **, $p < 0.01$.

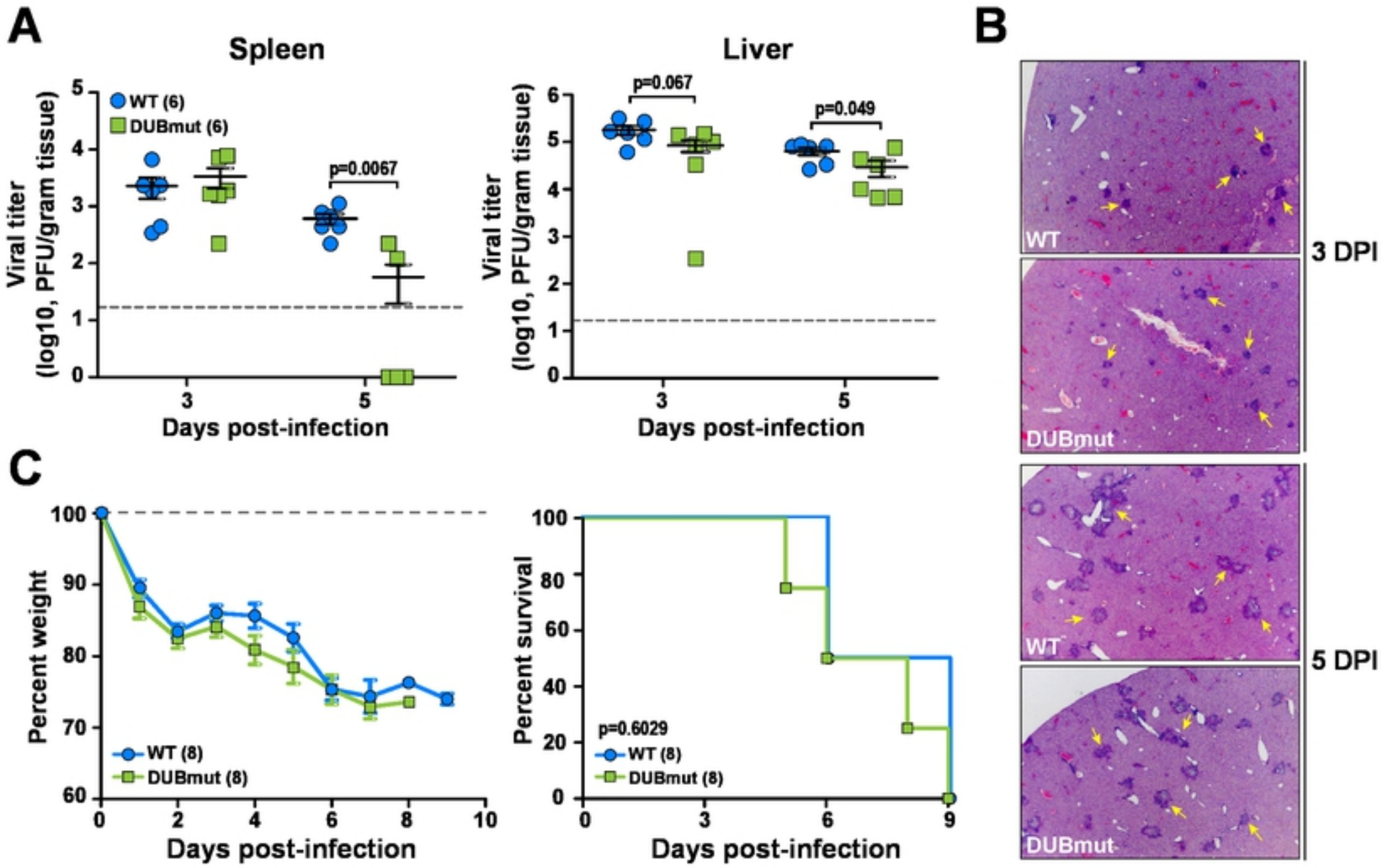

Figure 5. Evaluating replication and pathogenesis of MHV-DUBmut in mice. (A) Viral burden in livers and spleens isolated from WT- or DUBmut virus-infected mice was determined by plaque assay. The number of mice in each group is shown in parentheses. Data were statistically analyzed using unpaired t-tests and are presented as means ± SEM. (B) H&E staining of liver sections from infected mice at 3 and 5 days post-infection (DPI). Representative MHV-associated liver lesions are indicated by arrows. (C) Weight loss (left panel) and survival curve (right panel) of mice after intracranial inoculation with 100 pfu of WT or DUBmut virus. The number of mice in each group is shown in parentheses. Data were statistically analyzed using log-rank tests and are presented as means ± SEM.

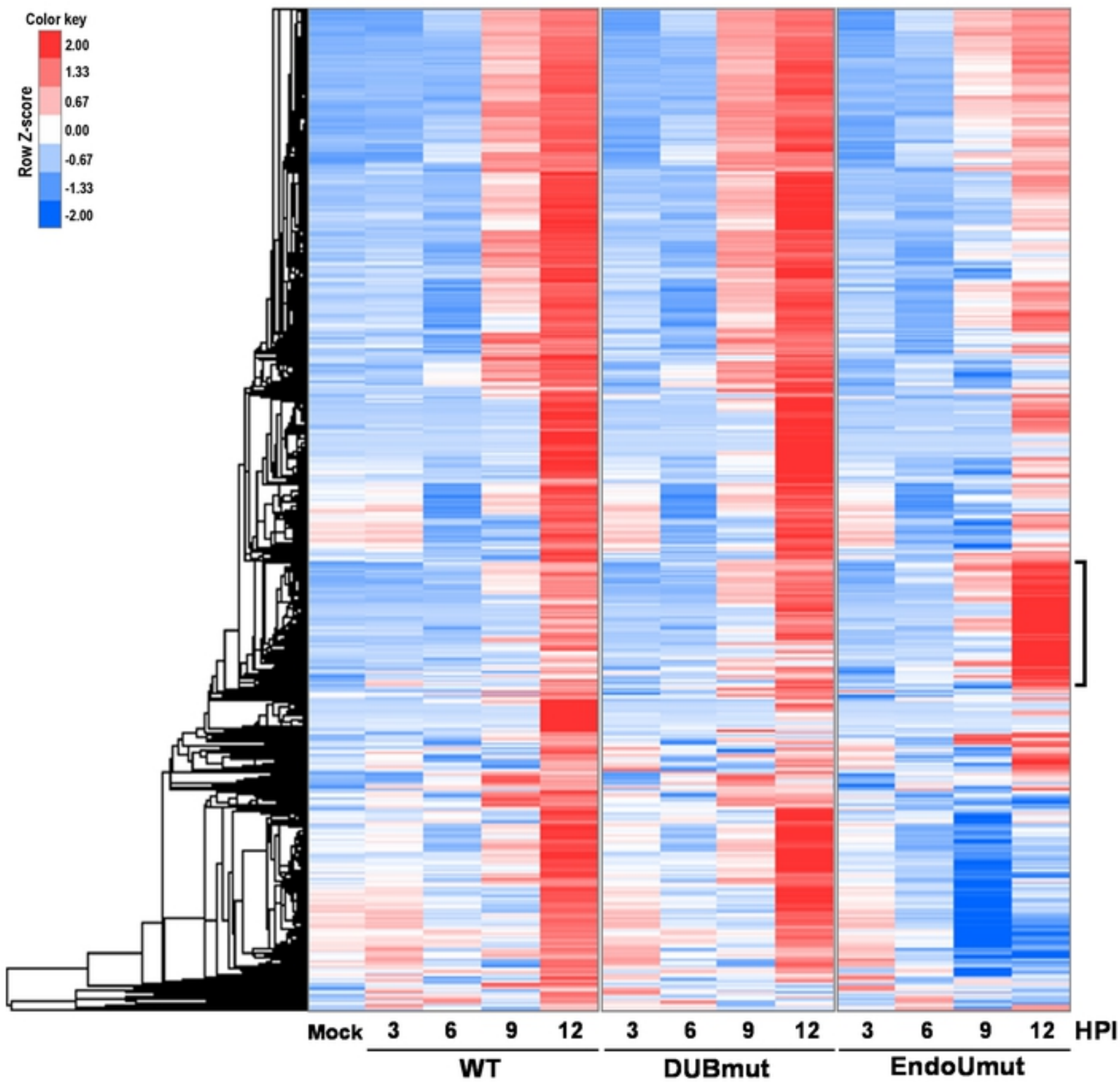

Figure 6. Global gene expression profiles from mock-, WT-, DUBmut-, and EndoUmut-infected BMDMs. Total RNA was extracted from mock- and virus-infected BMDMs at 3, 6, 9, and 12 hours post-infection (HPI). Samples were subjected to SR50 Illumina sequencing. Raw reads were processed to generate differential expression data and normalized counts for each gene in each sample. The expression data from WT MHV-infected BMDMs at 12 HPI was compared with mock-infected cells; a statistical significance cutoff of $q < 0.05$ and a fold-change cutoff of > 4 were applied to select the most highly statistically significant differentially expressed genes. The normalized counts for the 2,879 genes that met these cutoffs were averaged across replicates and converted to log2-transformed z-scores. These expression values were then imported into Cluster 3.0 software to mathematically arrange the gene list based on similarities in expression patterns between samples *via* the Pearson correlation (uncentered) and centroid linkage metrics. Java TreeView software was used to visualize the output from Cluster 3.0. Plotted are row z-score-standardized log2-transformed values for each gene across all samples and timepoints. The color bar indicates the approximate row z-score that is associated with each color, with warmer colors corresponding to higher relative expression values within each row and cooler colors corresponding to lower relative expression values. Bracket indicates the genes selected for subsequent analysis in Figure 7.

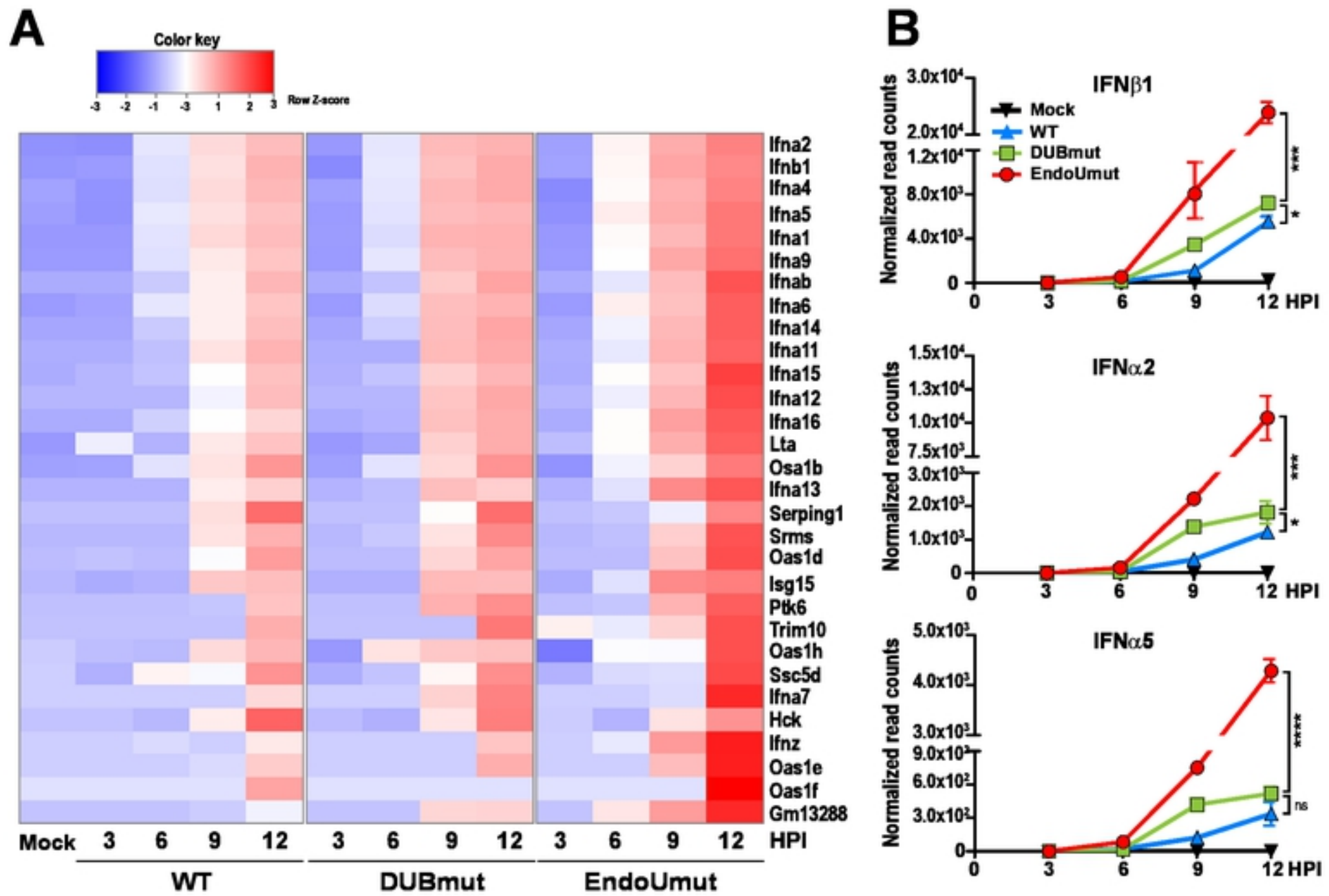

Figure 7. Expression profiles of genes identified by functional clustering (DAVID). After applying DAVID functional clustering to the data shown in Figure 6, the expression profiles of 30 genes within the cluster bracketed in Fig 6 were plotted as a heatmap and as line graphs to visualize the patterns of expression. (A) Plotted are row z-score-standardized log2-transformed means of replicates for all samples. (B) Normalized read count values for the most highly differentially expressed genes are plotted as line graphs (also see supplemental figures). Plotted are the average normalized counts for each gene in EndoUmut- (red), DUBmut- (green), WT MHV- (blue), and mock-infected (black) BMDMs infection groups over all four timepoints. The normalized counts from each infection group at 12 hours post-infection (HPI) were subjected to statistical testing using two-tailed Student's t-tests. *, $p < 0.05$; **, $p < 0.01$; ***, $p < 0.001$; ****, $p < 0.0001$; ns, not significant. Data are presented as means ± SD.

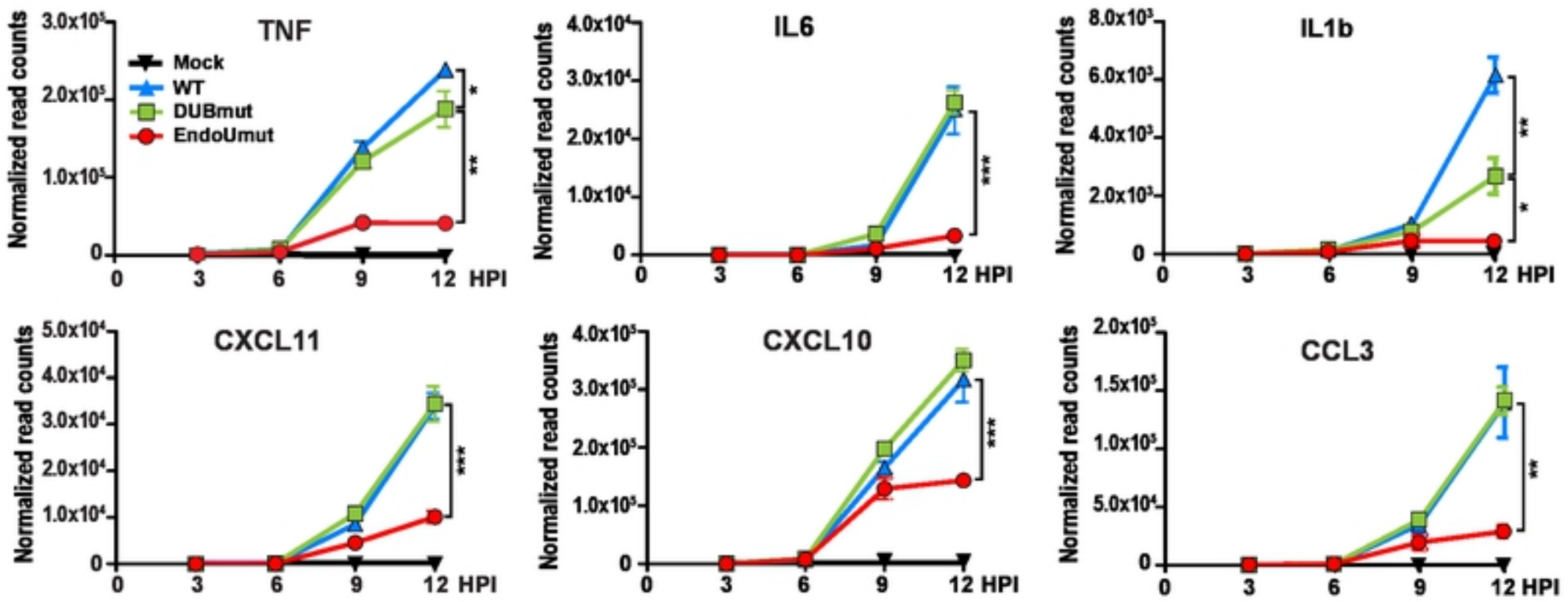

Figure 8. Expression profiles of NF-kappaB-mediated proinflammatory response genes identified by functional clustering (DAVID). Normalized count values for these genes are plotted as line graphs as described in Figure 7. Plotted are the average normalized counts for each gene in EndoUmut- (red), DUBmut- (green), WT MHV-(blue), and mock-infected (black) BMDMs infection groups over all four timepoints. The normalized counts from each infection group at 12 hours post-infection (HPI) were subjected to statistical analysis using two-tailed Student's t-tests. *, $p < 0.05$; **, $p < 0.01$; ***, $p < 0.001$; ****, $p < 0.0001$. Data are presented as means ± SD.

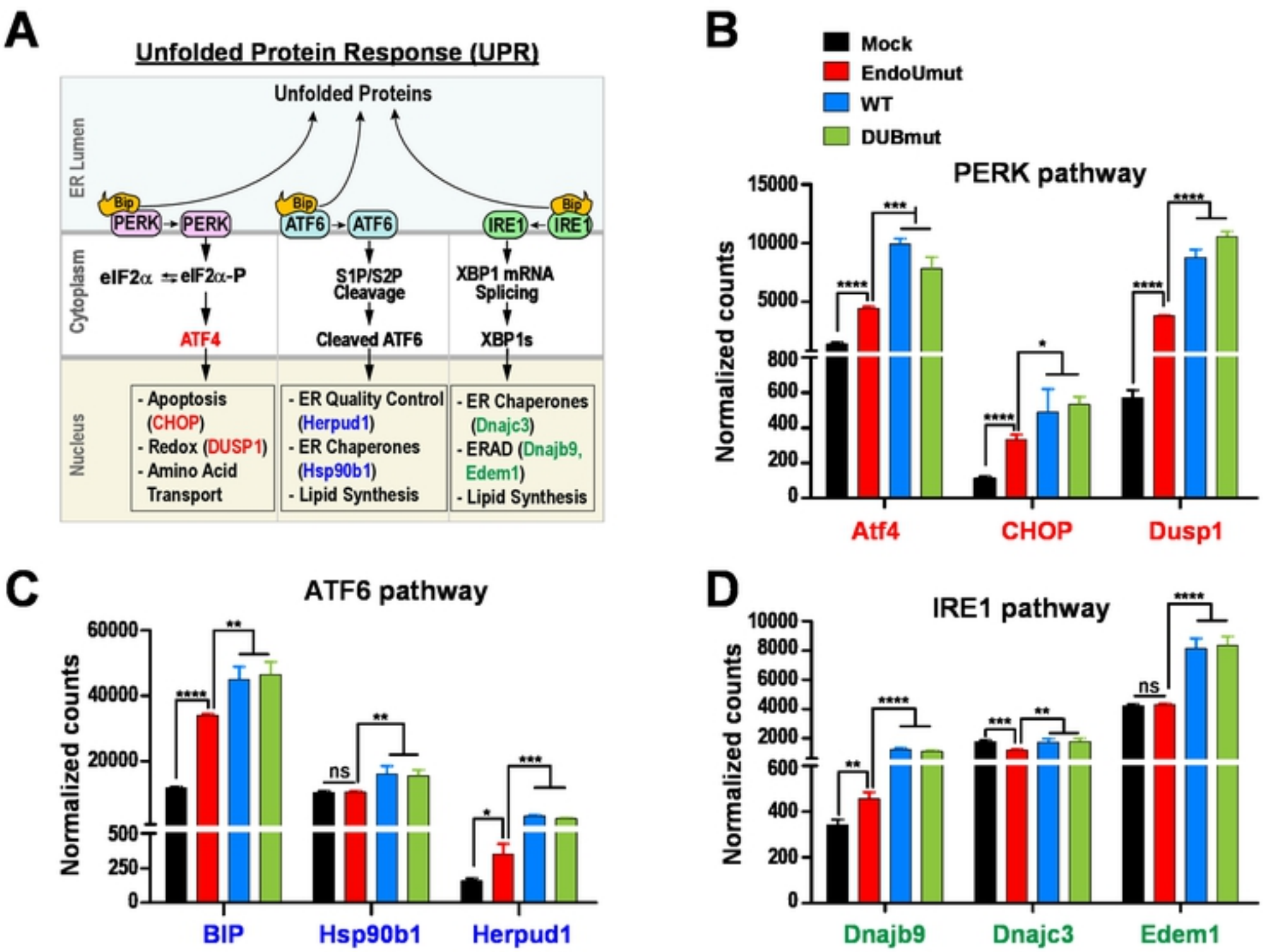

Figure 9. Expression of genes implicated in UPR pathways in WT MHV-, DUBmut-, and EndoU-mut-infected BMDMs at 12 HPI. (A) Schematic diagram of unfolded protein response. To evaluate the transcriptional response during viral infection, normalized count values for nine UPR-induced genes at 12 HPI are plotted. Genes are grouped into three panels according to whether their expression is triggered by (B) PERK, (C) ATF6, or (D) IRE1 pathway signaling. Data were subjected to statistical analysis using two-tailed Student's t-tests. *, $p < 0.05$; **, $p < 0.01$; ***, $p < 0.001$; ****, $p < 0.0001$; ns, not significant. Data are presented as means ± SD.